BROADBAND, POLARIZATION INSENSITIVE AND TUNABLE THZ METAMATERIAL ABSORBER USING GRAPHENE AND PHASE CHANGE MATERIAL

By

Nazia Homaira Preety
24371002

A thesis submitted to the Department of Electrical and Electronic Engineering in partial fulfillment of the requirements for the degree of
M.Engg. in Electrical and Electronic Engineering

Electrical and Electronic Engineering
BRAC UNIVERSITY

December 2024

Declaration

It is hereby declared that

1. The thesis submitted is my/our own original work while completing degree at BRAC UNIVERSITY.
2. The thesis does not contain material previously published or written by a third party, except where this is appropriately cited through full and accurate referencing.
3. The thesis does not contain material which has been accepted, or submitted, for any other degree or diploma at a university or other institution.
4. I have acknowledged all main sources of help.

Student's Full Name & Signature:

Nazia Homaira Preety

24371002

Approval

The project titled "Broadband, Polarization Insensitive and Tunable THz Metamaterial Absorber using Graphene and Phase Change Material " submitted by

1. Nazia Homaira Preety (24371002)

of Fall, 2024 has been accepted as satisfactory in partial fulfillment of the requirement for the degree of M.Engg. in Electrical and Electronic Engineering on 29/12/2024.

Examining Committee:

Supervisor (Chair of the Committee):

____

Abu S. M. Mohsin, PhD
Associate Professor
Department of Electrical and Electronic Engineering,
BRAC UNIVERSITY

Internal Examiner: (Member)

____

Saifur Rahman Sabuj, PhD
Associate Professor
Department of Electrical and Electronic Engineering,
BRAC UNIVERSITY

Chairperson (Ex officio):

____

Md. Mosaddequr Rahman, PhD
Professor and Chairperson
Department of Electrical and Electronic Engineering
BRAC UNIVERSITY

Ethics Statement

The study/research conducted for this project/thesis was performed as per university ethical standard. The outcome of this study is published in a renowned journal at DOI: 10.1016/j.heliyon.2024.e37973 and another article is under review. The similarity report suggested around 6% similarity (except self-citation)

Abstract/ Executive Summary

Metamaterials are artificially-engineered materials with features that are not easily evident in naturally occurring materials. They can be used for perfect lenses, invisibility cloaking, perfect absorption and transmission and other applications because they exhibit novel properties such as left-handed behaviour, a negative refractive index, a classical analog of electromagnetically-induced transparency, extraordinary transmission, negative Doppler effect and more. Metamaterial-based perfect absorbers are potential candidates for practical use as perfect absorbers. In this study, we looked at a novel strategy to build a graphene metamaterial (GMM) based terahertz (THz) absorber with dual-mode functionality, tunability and broadband absorption. We carried thorough simulations on four alternative configurations and observed the maximum absorption and its efficiency. The absorber is designed to work in two unique modes, increasing its suitability for various THz applications, by manipulating resonant structures and the materials. We also did detailed simulation on five distinct configurations of tuned resonant structures, which differed from those in the previous structures, and concluded that the optimized structure with phase change material (PCM) can accomplish bandwidth almost twice as large. Phase change materials are promising possibilities for electronic Flash memory. They are often utilized in commercial optical disks and rewritable media. Phase change material (PCM) is extraordinary compounds with unique switchable properties leading to an explosion of new applications in the field of electronics and photonics. Furthermore, the absorber is polarization insensitive, has a wide viewing angle and responds quickly. Metamaterial structures are mainly three layered. Two optimized structures of metamaterial absorbers have been proposed. This study gives insight into the new method that increases the high absorption width, as well as the great potential in the multifunctional modulator, considering with and without the phase transition material.

Our primary goal is to design a graphene-based metamaterial absorber that can achieve near unity frequency absorption that has maximum bandwidth. We have designed simple structure compared to the existing hybrid absorbers that can give nearly frequency bandwidth 7.69THz dualband and multiband absorption. Furthermore, we demonstrated step-by-step reliable methodologies to the fabrication of graphene-based metamaterial.

Keywords: Metamaterial, THz absorber, graphene, phase change material, vanadium dioxide (VO_2), bandwidth and absorptivity.

Acknowledgement

I would like to express my gratitude to my supervisor, Dr. A. S. M. Mohsin, Associate Professor, Department of Electrical and Electronic Engineering, for his enormous recommendations, guidance and assistance throughout the process. I would also want to thank the outstanding academics and the staff of the Department of Electrical and Electronic Engineering at BRAC UNIVERSITY for their long-standing assistance and collaboration.

In addition, I would like to take this occasion to express my gratitude to everyone who has helped me succeed at BRAC UNIVERSITY.

List of Publications

I. **Nazia Homaira Preety** and Abu S.M. Mohsin, **"Graphene metamaterial (GMM) based dual mode, tunable, and broadband THz absorber with triple circular split ring structure"**, Heliyon, (Q1,IF4.0,Citescore 4.5), DOI: 10.1016/j.heliyon.2024.e37973

II. **Nazia Homaira Preety** and Abu S.M. Mohsin, **"Graphene- Vanadium Dioxide (VO_2) Based Wideband Tunable Polarization Insensitive THz Absorber Using Fishnet and Circular Split Ring Structure"**, (Under Review).

Table of Contents

List of Tables

List of Figures

List of Acronyms

NIM	Negative Index Material
DNG	Double Negative
LH	Left Hand
BW	Bandwidth
TM	Transverse Magnetic
TE	Transverse Electric
GMMA	Graphene Based Metamaterial Absorber
MMPA	Metamaterial Based Perfect Absorber
EM	Electromagnetic
SP	Surface Plasmon
PEC	Perfect Electrical Conductor
FDTD	Finite Difference Time Domain
CVD	Chemical Vapour Deposition
ALD	Atomic Layer Deposition
DBMA	Dielectric Based Metamaterial Absorber
GPCM	Graphene Based Phase Change Metamaterial

Chapter 1

Introduction

1.1 Background

Metamaterials are artificially structured materials engineered to have properties not found in naturally occurring materials. They gain their unique properties from their structure rather than their composition. Metamaterial absorbers are a specific type of metamaterial designed to absorb electromagnetic waves across a range of frequencies, including microwave, terahertz, infrared, and optical frequencies. It has gained popularity due to its 3D structure that comprised of at least two different materials, with a response or function that impossible to achieve with any individual constituent material. All natural materials, like glass and diamond, exhibit positive values for electrical permittivity, magnetic permeability, and the index of refraction. In contrast, these newly engineered materials, known as negative index materials (NIM), double negative (DNG) media, left-handed (LH) materials, or backward wave media, have negative values for these parameters. These unique characteristics enable the development of innovative, compact antennas and microwave components/devices for use in wireless communications and defense industries [1].

As material science progressed, photonic materials were developed that use the photon of light as the primary transport of information. This has led to photonic crystals, and at the beginning of the new century, the proof of principle for working metamaterials with a negative index of refraction in the microwave (at 10.5 gigahertz) and optical ranges. Natural materials exhibit only a limited range of electromagnetic properties compared to what is theoretically possible. To address this, researchers have extensively explored the development of new materials with specific, desired properties.

Electromagnetic metamaterials are artificially engineered to manipulate and control electromagnetic waves in innovative ways [2]. Photonic metamaterials, which are periodic optical nanostructures typically made of metallic elements on dielectric or semiconducting substrates, have periods shorter than the wavelength of light [3]. Moreover, graphene is gaining recognition as a promising material for ultrathin, highly efficient light absorption due to its exceptional optical properties. With its remarkable electrical, thermal, mechanical and optical characteristics, derived from its unique band structure, graphene holds significant potential for various terahertz applications. Researchers have addressed the constraints of biosensors, which are often limited by resonance frequency and bandwidth, by utilizing phase change materials (PCM). These materials can alter their state and properties in response to extent factors like temperature or pressure. By combining phase change material with metamaterial absorbers, it becomes possible to develop dynamic, tunable and reconfigurable photonic devices.

1.2 Motivation

Metamaterials, with their ability to manipulate electromagnetic waves in the unprecedented ways, have revolutionized the field of material science and photonics. Among the most exciting advancements are tunable metamaterial, which open up possibilities for dynamic control of electromagnetic properties. This tunability has led to groundbreaking applications such as, optical image sensing, sensing, EM detection, THz switching, super lens, absorber, invisibility cloaking, sound filtering, more efficient solar absorption and more. The development of such metamaterial addresses critical challenges in a variety of fields, including enhancing the efficiency of renewable energy sources and futuristic stealth applications. Exploring this topic not only expand our understanding of electromagnetic wave manipulation, but also inspires novel solutions to real-world problems.

Although metamaterial absorbers offer various advantages, they typically have a narrow bandwidth. To enhance the absorption bandwidth, metamaterial absorbers with multiple dielectric layers are used, but their significant thickness poses a major limitation for many applications. Wideband absorbers have been proposed using multi-resonant structures, which combine several resonant elements to achieve greater absorption bandwidth [4]. However, these absorbers are often large in size and challenging to control at each absorption frequency. Therefore, this article proposes Tunable Graphene Metamaterial Absorber which can obtain unity absorption with larger bandwidth compared to the conventional absorber in all aspects. We have tried to optimize the metal-insulator-metal (MIM) structure and also modified the cell structure to overcome the problem of narrow bandwidth to achieve dual and multiband absorption in THz range. This article is a project-based work that shows the simulation results of the metamaterial cell with the equivalent circuit theory and its fabrication process.

1.3 Literature Review

Metamaterial, which are engineered metamaterial with properties not found in nature, have garnered significant interest in the terahertz (THz) frequency range due to their unique electromagnetic characteristics. Among these, THz metamaterials absorbers are particularly important for applications in imaging, sensing and communication systems. Recent advancements in the design and functionality of metamaterial-based THz absorbers have surpassed earlier innovations. These improvements include the use of various resonator shapes, such as split-ring resonators (SRRs), complementary SRRs, and multi-layer configurations, aimed at enhancing absorption bandwidth and efficiency.

Single-band high-absorption metamaterial absorbers (MMAs) are often unsuitable for many applications [5]. Consequently, researchers have shifted towards the development of wideband or multiband and high efficiency is challenging because the conditions for perfect absorption are highly sensitive and easily disrupted. This ongoing challenge has driven research efforts, including our own. The incorporation of active and popular materials like graphene, phase change material and GST/IST compounds has enabled dynamic tuning capabilities, improving absorber performance. Graphene's tunability via external bias allows real-time control over absorption frequencies, while materials like vanadium dioxide (VO_2), which can transition between insulating and metallic phase, enable adaptive adjustment of absorption properties.

Since the introduction of the split-ring resonator based perfect MMA by Landy et al. in 2008 [6] substantial research has been devoted to this area, resulting in various innovative MMAs. For instance, Zhonglei Shen et al. developed a THz absorber with a pagoda-like structure using gold, resin and quartz. Their design achieved unity absorption, though the bandwidth was limited to 1.81 THz (from 1.07 to 2.88 THz) [7]. Similarly, S. Banerjee et al. proposed a swastika-shaped design made of gold on a gallium arsenide (GaAs) substrate, achieving nearly perfect absorption (99.65%) at 2.905 THz, with a quality factor (Q-factor) of 145.25, but has limited bandwidth [8]. Additionally, Zianfei Zhu et al. introduced an ultra-broadband, polarization-insensitive, wide-angle THz MMA using truncated pyramid unit structures in a metal-dielectric multilayer composite [9]. This design demonstrated absorption above 80% over the range of 0.7 to 2.3 THz, with performance maintained up to 40° incident angle.

Despite the advancements, most THz based designs still fail to achieve absorption bandwidths beyond 3 THz. To address this limitation, we have developed graphene-based THz metamaterial absorber expected to achieve near unity absorption over frequency bandwidths exceeding 3 THz, providing significant larger bandwidth than previously reported designs.

1.4 Objectives with specific aims and possible outcome:

Our primary goal is to achieve a wide frequency bandwidth with absorption exceeding 90%. A larger bandwidth enables the absorber to operate effectively across a broader range of frequencies, enhancing its suitability for various applications. The Objectives of this thesis are:

- Achieve the highest bandwidth for maximum efficiency.
- Optimized tunable metamaterial structure for broad frequency range.

- Observe the trend of absorption in different wavelengths.
- Observe the influence of structural parameters change with different metals and graphene.

Specific Outcome:

- Create a graphene based tunable metamaterial structure that achieves ultra-broadband absorption.
- Develop an optimized, simple and tunable structure that gives the maximum absorption.
- To verify the desired absorption spectrum non-normal incident angles, wavelength and frequency range.

1.5 Outline of Methodology/Experimental Design:

A comprehensive study of different cases of metamaterial absorber has been studied and the results have been shown in details. Different cases are presented here and two different final structures are proposed for our desired outcomes.

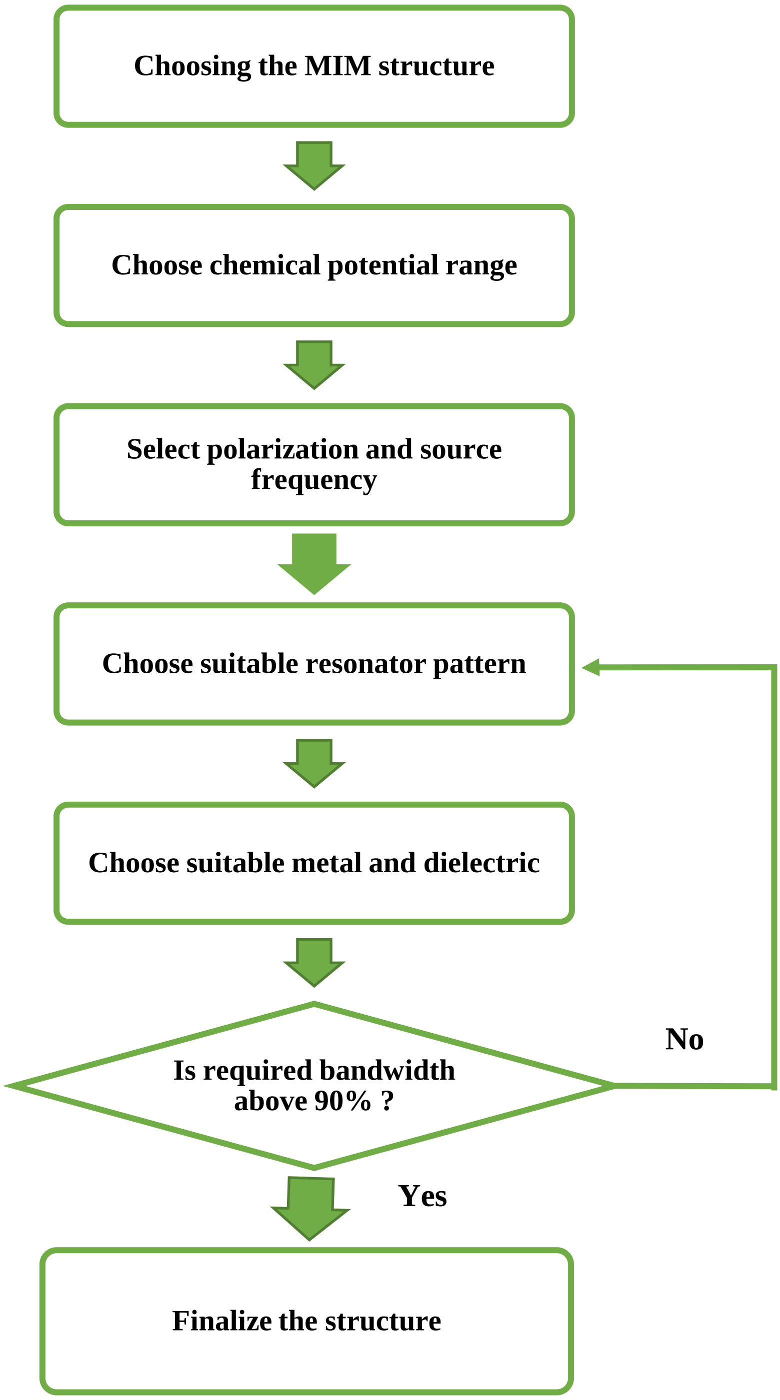

Figure 1.1: Steps of designing the metamaterial structure.

We have chosen a simple structure from a number of investigations based on the application of metamaterial absorber. With specific structure parameters, a simple metal-dielectric-metal and a dielectric-metal-dielectric containing graphene is chosen. Next, choose the source frequency and polarization angle that will produce the most output. Subsequently, we set distinct chemical potentials from 0.1eV to 0.9eV. Selecting the top layer structure that will resonate at the applied frequency is the next stage. In this case, several distinct architectures were examined that produce various absorbance curves. Here, the source polarization and central frequency is very important to observe which frequency is best for the selected cell. Next, it becomes easy to study the effects of the resonant patterns and optimize the size of the overall structure. We settled on a structure and continued to improve it in order to attain optimum absorption and larger bandwidth after a few tweaks until we find our desired outcomes. In this step, we chose the structure of to optimize area and simulated further with best suited materials. Finally, the simulation is carried out with different metals and compounds like tungsten, gold vanadium, some GST and IST etc to compare the absorption in each case. The simulation is done in Ansys Lumerical Finite Difference Time Domain.

1.6 Thesis Structure

Chapter 1 provides an introduction to metamaterial absorbers and reviews terahertz-based metamaterial absorbers. We evaluated their results to identify improvement areas and set our objectives. The chapter also outlines the design methodology and details the optimization process. Finally, the thesis structure is summarized.

In Chapter 2, we described the design methodology for the MIM (metal-insulator-metal) structure of the metamaterial absorber. This includes analyzing four different structure incorporating graphene, metal and (SiO_2) silicon dioxide. We presented the simulation conditions, circuit theory, and fabrication process, along with a comparison of results to similar prior works.

Similarly, Chapter 3 examines metamaterial absorber designs using phase change materials, presenting five configurations involving VO_2, graphene and SiO_2. Then, this chapter discussed the simulation setup, equivalent circuit, results, and fabrication process.

Finally, Chapter 4 summarizes the experimental findings, confirming that the objectives were met. We also addressed challenges in the development of metamaterial absorbers and discussed potential directions for future work.

Chapter 2

Graphene Metamaterial (GMM) Based Dual Mode, Tunable and Broadband THz Absorber

2.1 Introduction

In this study we investigated a novel approach to designing a graphene metamaterial (GMM) based terahertz absorber with dual-mode functionality, tunability, and broadband absorption capabilities. The study leverages the unique properties of graphene, a material known for its exceptional electronic and optical characteristics, combined with metamaterials to achieve efficient THz absorption. Here we performed extensive simulation on four different types of configurations and found the optimized structure has the highest bandwidth of 3.8 THz and absorption over 90%. The absorber is designed to operate in two distinct modes, enhancing its versatility for different applications in the THz spectrum. Moreover, the tunability of the absorber is a significant feature, allowing for dynamic adjustment of the absorption frequency, which is crucial for applications in THz imaging, sensing, and communication systems. The broadband nature of the absorber ensures effective performance over a wide range of frequencies, addressing the need for flexible and high-performance devices in emerging THz technologies. This work represents a significant advancement in the field of THz metamaterials, with potential implications for the development of next-generation THz devices.

2.2 Literature Review

Metamaterials (MMs) are artificially crafted materials engineered to possess unique characteristics. They can be structured as regularly arranged composites in two or three dimensions, showcasing distinctive properties across a spectrum from microwave to optical frequencies [10]. The exploration of metamaterials extends its scope across various fields, including electromagnetics, optics, optoelectronics, and solid-state physics. Terahertz metamaterials represent a sophisticated class of composite structures engineered to interact within the terahertz frequency spectrum, typically defined as 0.1 to 10 THz. These materials can be precisely tailored to elicit a customized electromagnetic response by adjusting the geometry and dimensions of their constituent structural units. Their sensitivity to environmental factors has made them instrumental in the detection of diverse analytes. The terahertz frequency domain, situated between microwave and infrared frequencies, is often referred to as the sub-millimeter wavelength range. Despite the inherent challenges in propagating terahertz waves through the atmosphere—limiting their commercial exploitation—these frequencies hold immense promise in scientific applications such as remote sensing and spectroscopy. The exceptional attributes of these structures, including high absorptivity, robust tunability, and wide-angle absorption, position them as pivotal in advancing fields like terahertz sensing, nondestructive evaluation, imaging, stealth technology, and detection systems. Consequently, terahertz metamaterials are poised to play a critical role in security screening, medical imaging, wireless communication systems, nondestructive testing, chemical identification, and sub-millimeter astronomy [11] . Within the realm of materials science, graphene has emerged as a focal point owing to its extraordinary mechanical, electrical, and optical characteristics [12]. Meanwhile, graphene has the highest mobility in known materials, and its conductivity can be tuned by electrochemical potential. Metamaterial-based perfect absorbers (MMPAs) are promising candidates for the practical application of perfect absorbers [13]. An MMPA typically consists of three layers. The first layer features periodically-arranged metallic patterns, with structures and geometric parameters precisely adjusted to meet the impedance-matching condition with the surroundings, ensuring no reflection of incoming electromagnetic waves. The second layer is a dielectric layer, providing a space for EM wave dissipation and sometimes acting as a resonance cavity to extend the duration of the EM waves within the layer. The third layer is a solid metallic plate that prevents any remaining transmission. For practical applications, several factors of MMPAs must be carefully considered, including broadband operation, polarization-independent response, omni-directional response, and tunability. These characteristics are primarily determined by the MMPA's structure. Additionally, flexibility is a crucial factor, influenced by the materials used in the fabrication process.

Graphene transcends its mechanical and electrical properties, demonstrating exceptional utility as a two-dimensional platform capable of sustaining surface plasmons (SPs) within the infrared and terahertz spectra. This distinctive capability enables robust confinement of electromagnetic fields at sub-wavelength scales, rendering graphene an ideal substrate for crafting metamaterial absorbers achieving complete absorption in THz. Metamaterial-based devices, known as MMAs, have garnered considerable attention due to their innovative design and versatile functionality. These advanced constructs transcend conventional applications, serving as sophisticated sensors, integral components in state-of-the-art detection systems, and fundamental elements in high-resolution imaging apparatus. The investigation and validation of MM properties, in conjunction with the utilization of terahertz spectroscopy, have emerged as a burgeoning area of focus in contemporary scientific inquiry. In the case of THz absorbers, graphene extraordinary features resulted in a surface Plasmon polariton-based absorption [14]**.** Highlighting the gap, achieving impedance matching with the methods outlined in prior research poses significant challenges and complexities. For instance, determining the central frequency of absorption in the terahertz range remains elusive. These constraints limit the design process and diminish efficiency, as highlighted in the work by S. Reza. Moreover, at elevated frequencies within the THz spectrum, fulfilling the conditions for impedance matching becomes increasingly arduous. Given the inherent challenge of identifying effective absorption materials within the THz spectrum from natural sources, the strategic development of THz MMAs assumes paramount importance. In recent years, numerous studies have emerged,

delineating the applications of MMAs in various electromagnetic (EM) fields such as stealth technology, detection mechanisms, modulation techniques, and imaging systems. Terahertz waves, occupying a segment within the electromagnetic spectrum, pose practical challenges for direct detection, necessitating measurement through either wavelength or energy periodicities.
It has been shown by Rhee et. el. that metamaterials hold significant potential in the terahertz regime, leading to the development of various THz MM devices. These include perfect absorbers, amplitude and phase modulators, waveguides, devices utilizing electromagnetically induced transparency, broadband THz generators and detectors, and antennas. Presently, scientific inquiry has introduced an innovative methodology, which capitalizes on graphene in tandem with an external bias voltage to precisely modulate the absorption characteristics of Terahertz Metamaterial Absorbers.

Landy et al. were the first to propose a metamaterial absorber, which featured advantages such as smaller size and thinner thickness compared to conventional absorbers [6, 15]. Since their groundbreaking work, numerous optimized MM absorbers have been developed for various applications, including thermal imaging [16, 17], solar cells, and sensors. These optimizations encompass multiband [18, 19], broadband [20, 21], polarization-independent [5], and tunable band absorbers [22]. However, integrating multiband MM absorbers with high efficiency remains challenging due to the delicate conditions required for perfect absorption. This continues to be a significant focus in MM absorber research. Despite extensive studies, many challenges persist, such as relaxing the operational conditions, increasing the number of absorption peaks and bandwidth [23], and transitioning absorption properties from microwave to infrared (IR) frequencies [24]. Zhang S. et.al. showed a variety of metallic nanostructure designs in their article, such as split-ring resonators, cut wire antennas, and fishnet structures, have been utilized to develop metamaterials and metasurfaces with optical properties that surpass those of natural materials and their interfaces [25]. Although metallic nanostructures provide unparalleled performance in subwavelength light concentration, they experience significant intrinsic absorption losses at optical frequencies, which greatly reduce their efficiency [26]. Yuandan Dong and Tatsuo Itoh proposed metamaterial-based small antennas as a method to manipulate the dispersion relation or near-field boundary conditions, potentially leading to antenna miniaturization while preserving optimal radiation performance by introducing 4 different categories [27]. Numerous metamaterial designs documented in the literature exhibit behaviour such as diamond-shaped, cross-shaped nanoresonators [28], square, circular, and cross-shaped metal-resonators [29], fishnet [30] spiral, ring, disk, square [31] and many others for various applications. Additionally, metamaterials are categorized into several distinct classes based on their modified properties, including thermal, acoustic/transport, electromagnetic, and mechanical [32]. However, many designs necessitate via the substrate, resulting in complex structures with large unit cell dimensions.

M. J. Hossain, M. R. I. Faruque, and M. T. Islam examined a perfect metamaterial absorber (PMA) with high fractional bandwidth (FBW) [33]. In their article, they have proposed a basic PMA structure which gives almost 99.96% and 99.60% perfect absorption at 523.84 THz and 674.12 THz resonance frequencies. However, from the data given, the absorption varies drastically within the bandwidth which varies from 70%-99%. Although this result is obvious for metamaterials, it just gives the overall idea of probable obtainable energy in a very wide range of frequencies. C. S. R. Kaipa et. al. examined the transmission behaviour observed in these graphene-dielectric stacks is similar to that of wire mesh grid-dielectric stacks [34]. The features of the bandpass region, characterized by transmission peaks in the spectra, are explained by Fabry-Pérot resonances, analogous to those previously identified in wire mesh grid-dielectric stacks at microwave frequencies. Like the previous article, this examination also gives the overall idea of lower THz bandwidth but not the accurate efficiency at that bandwidth. The above works gave excellent results in terms of wideband and near perfect absorption but the results show frequent drop to almost 50% of absorbance. Furthermore, the graphene layer must be thick (h=150μm) during fabrication, which is an area issue. These can be further analysed and improved to get better absorption and accurately measure lower or higher bandwidth using the concept of tunable graphene absorber. Although the above proposed works have multiband features, it still has the problem of difficulty in achieving perfect absorption. There are persistent challenges, such as the limited interaction of terahertz waves with most natural materials, and the low spatial resolution or limited confinement of terahertz devices due to the diffraction limit in terahertz metamaterial sensing applications. The major limitations of these absorbers are their large size and the difficulty in controlling the structure at each absorption frequency. To fill the gap in the literature, we propose to create a graphene dielectric-based metamaterial absorber with a longer bandwidth and higher absorption. To do this, we evaluated four types of metamaterial structures and discovered a broadband spectrum with a bandwidth of 3.4 THz at 90% efficiency, encompassing the 1.1 THz to 4.9 THz range. The proposed metamaterial structure will provide a new avenue in several applications such as energy harvesting, photothermal solar cells, THz antenna design, stealth technology, photodetector, THz imaging imaging and sensing.

2.3 Structural Design and Methodology

We studied four different cases and their results have been compared. Figure 2.1 shows the top view of all 4 of the cases.

2.3.1. Case-1: Fishnet Structure

Figure 2.1 (a) is the structure of the first case absorber where the absorption spectrum can be tuned by changing the chemical potential applied to the graphene. The top unit cell has a fishnet structure of grapheme and rectangular structure of refractive index 1.53. The bottom layer has a refractive index of 1.43. A background index of 1.53 was used. The top unit consists of the following dimension: g1=2μm, w1=1.5 μm, P=18 μm, P1 & P2=6.5 μm.

2.3.2. Case-2: Fishnet + Circular Split Ring

This is almost similar structure to the Case-1, except a circular split ring is introduced. The refractive indices are similar to Case-1 as well. The dimension of the rectangular split structures are the same as that of Case-1 (shown in Figure 2.1 b). The circular split ring consists of: a=20^{o} gap, b=1.7 µm, r=6 µm, g1=2µm, P=18 µm, P1=6.5 µm, P2=6.5 µm.

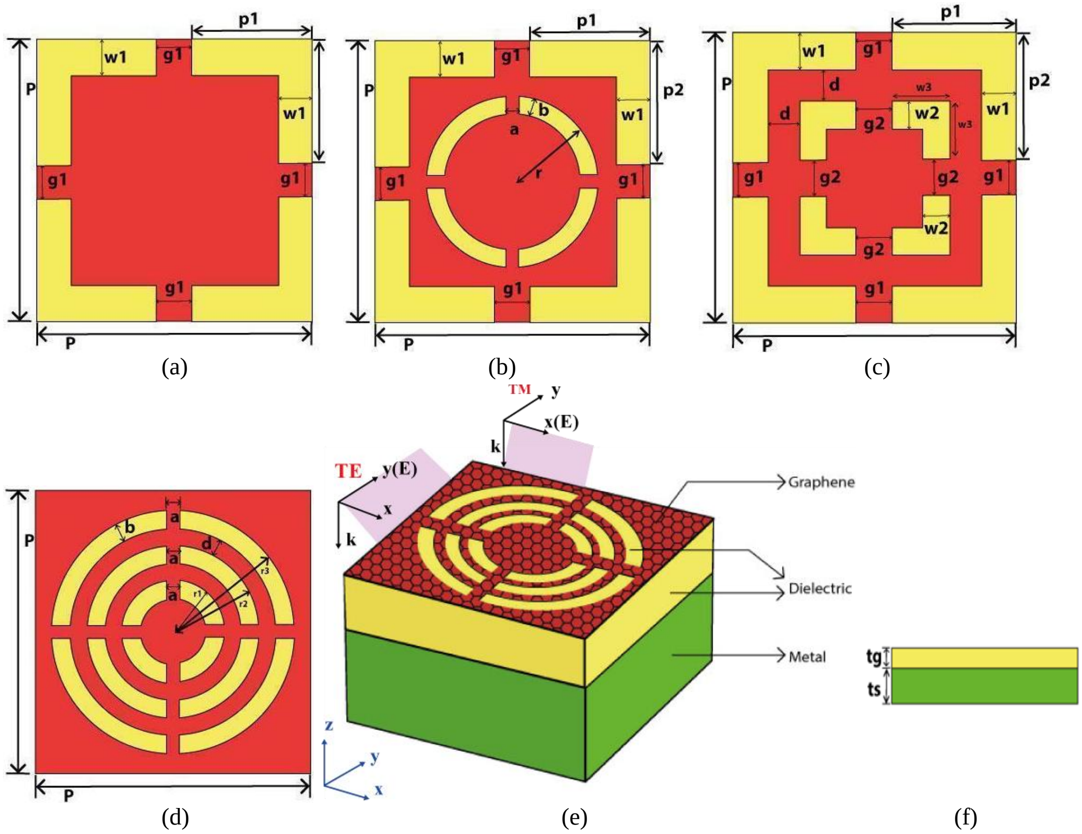

Figure 2.1: (a) Top view of the structure in Case-1 (Fishnet structure), (b) Top view of the structure in Case-2 (Fishnet + Circular Split Ring), (c) Top view of the structure in Case-3 (Fishnet+Rectangular Split Ring), (d) Top view of the structure in Case-4, (e) Perspective view of the structure in Case-4 (Triple Split Rings), (f) Side view (x-z) of all the unit cell. Green=Metal and Yellow= Silicon dioxide.

2.3.3 Case-3: Fishnet + Rectangular Split Ring

In this structure there are 2 rectangular split rings with the same thickness and splits as shown in Figure 2.1 c. The dimension of the top cell is as follows: P=18 µm, P1=6.5 µm, P2=6.5 µm, g1=2µm, g2=2µm, w1=1.5 µm, w2=1.5 µm, w3=3.5 µm, d=1.5 µm.

2.3.4 Case-4: Triple Circular Split Rings

Unlike the other cases, in Case-4, three circular split rings have been introduced with no rectangular split rings. Figure 2.1 (e) shows the 3D perspective view of the structure with all three layers. The dimension of the top unit shown in Figure 2.1 (d) is as follows: P=18 µm, b=1 µm, a=20° gap, d=1 µm, r1= 3 µm, r2= 5 µm, r3=7 µm.

The Figure 2.1 (e) is the proposed structure that displays the 3D and the top view structure, respectively, of Graphene Metamaterial Absorber unit cell, while the evolution of its structure is depicted in the supplementary material. The absorber consists of three layers: the upper one features a graphene design, while the lower layer is a dielectric made of SiO_2 with a relative permittivity (ε) of 1.43. Here SiO_2 provides support for the absorber while minimizing circuit capacitance and dielectric losses, thus improving signal quality and transmission speed. Lastly, in the lower structure is metal. Arc shapes with a refractive index of 1.53, representative of the background index for dielectric, were employed to structure the 2D graphene sheet in the fishnet design. It also offers resistance to moisture absorption and maintains high thermal stability, safeguarding electrical performance against humidity and temperature fluctuations. Moreover, SiO_2 demonstrates minimal dielectric dispersion, ensuring a consistent dielectric constant across various frequencies. The thickness of the metal and SiO_2 layers is represented by t_s and t_g, respectively, as shown in Figure 2.1(f).

Table 2.1: Dimension of proposed 4 structures

Sl	**Structure Parameter**	**Case 1: Fishnet (μm)**	**Case 2: Fishnet + Circular split Ring(μm)**	**Case 3: Fishnet+ Rectangular Split Ring(μm)**	**Case 4: Triple Circular Split Rings(μm)**
1	Top side layer (Dielectric 1.53)	L(p1)=6.5, W(p2)=6.5, Thickness w1=1.5, H=1.	L(p1)=6.5, W(p2)=6.5, Thickness w1=1.5, H (both rect & circ)=1, Width of ring b=1.7, Outer radius r=6.	L(p1)=6.5, W(p2)=6.5, Thickness w1=1.5, H (both rectangular)=1, Width of 2nd ring w1,w2=1.5, w3=3.5.	Outer radius r1=3, Outer radius r2=5, Outer radius r3=7, Width b=1, H (all 3)=1.
2	Top middle layer (2D graphene sheet)	L=20, W= 20	L=20, W=20	L=20 , W=20	L=20 , W=20
3	Bottom layer (Metal 1.4)	L=18, W= 18 H=35.9	L=18, W= 18 H=35.9	L=18, W= 18 H=35.9	L=18, W= 18 H=35.9

The optimal unit cell size is P µm × P µm (with P = 32 µm). Our target, the absorption coefficient (A) was then computed using the formula,

$$A = 1 - |S_{21}|^2 - |S_{11}|^2 \quad (2.3.1)$$

$$= 1 - |S_{11}|^2$$

$$= 1 - S$$

where transmission (S_{21}) (also called T) and reflection $R = S_{11}$.

The contribution of transmission (S_{21}) was disregarded due to the inhibitory effect of the absorber's substrate. The presence of the absorber's substrate results in a reduction or prevention of electromagnetic wave transmission, indicating an inhibitory effect on the absorber's function.

The level of absorption can be determined by utilizing the Poynting vector, which indicates the power flow of an electromagnetic wave. The Poynting vector is given by **S** = **E** × **H**, where **E** is the electric field and **H** is the magnetic field. The absorption per unit area is then given by $A =$

$-1/2\mathrm{Re}(\mathbf{K}\cdot\mathbf{E})$, where **K** is the surface current density and Re denotes the real part. This formula shows that the absorption depends on the magnitude and phase of the surface current density relative to the electric field of the incident wave. So, to accurately model the EM behaviour, open boundary conditions to the simulation model. Periodic boundary conditions are established in the z-direction to allow for infinite extension of the simulation space, while periodic boundary conditions are applied along the x and y directions, ensuring periodic repetition of the simulation unit. These boundary condition choices collectively contribute to a thorough depiction of electromagnetic interactions within the simulated environment, thereby augmenting the precision of the simulation outcomes. This research focuses on investigating the nuanced dynamics of transverse electric (TE) waves within the realm of electromagnetic interactions. The TE waves, distinguished by their perpendicular alignment to the propagation axis, play a crucial role in the study. The investigation focuses on the *x*-*z* incident plane, with specific attention to the azimuthal angle φ, set at 0°, defining the orientation of the incident TE wave within the *x*-*y* plane.

The permittivity of graphene (ε_g) can be expressed by the following equation [34]:

$$\epsilon_g = 1 + j\frac{\sigma(\omega)}{\epsilon_0 \omega tg} \tag{2.3.2}$$

where, ω = angular frequency

tg = thickness of graphene layer

ε_0 = permittivity in a vacuum environment

(ω) = complex surface conductivity of graphene

The surface conductivity of graphene $\sigma(\omega)$ is typically a combination of intra-band conductivity and inter-band conductivity. In the terahertz to optical frequency range, the complex surface conductivity $\sigma(\omega)$ of graphene can be characterized by Kubo formula [35]:

$$(\omega, \mu c, \Gamma, T) = \sigma_{\text{intra}}(\omega, \mu c, \Gamma, T) + \sigma_{\text{inter}}(\omega, \mu c, \Gamma, T)$$

$$= -\frac{ie2kBT}{\pi\hbar^2}\left[\frac{1}{(\omega + i2\Gamma)^2}\int_0^{\infty} d\epsilon \left(\frac{\delta nF(\epsilon)}{\delta\in} - \frac{\delta nF(-\epsilon)}{\delta\in}\right)\in - \int_0^{\infty} d\epsilon\, \frac{nF(-\in) - nF(\epsilon)}{(\omega + i2\Gamma)^2 - 4(\frac{\varepsilon}{\hbar})^2}\right] \quad (2.3.3)$$

where, σ_{intra} and σ_{inter} respectively stand for intraband and interband conductivities, denoting the conductivity within a specific energy band and between different energy bands. The following symbols denotes as,

e = charge of an electron,

$\hbar$ = reduced Planck's constant in quantum mechanics

= energy of the charge carriers

Furthermore, Γ = 5 meV represents the scattering rate of charged particles, indicating the frequency at which these particles undergo scattering events, with a specified value of 5 meV. The Fermi-Dirac distribution function n_F describes the probability of finding a fermion with energy ϵ in a system at room temperature T = 300K is

$$n_F(\epsilon) = \frac{1}{1+exp\,(\frac{kBT\,(\epsilon - \mu_c)}{kBT})} \quad (2.3.4)$$

where kB is Boltzmann constant and ω represents the radian frequency in wave-related contexts and μc denotes the chemical potential of graphene.

The approximate value of σ_{intra} and σ_{inter} can be calculated analytically by the following equations [33]:

$$\sigma_{intra}(\omega, \mu_c, \Gamma, T) \approx i\frac{e^2 k_B T}{\pi\hbar(\omega + i2\Gamma)}\left[\frac{\mu_c}{k_B T} + 2ln\left(e^{-\frac{\mu_c}{k_B T}} + 1\right)\right] \quad (2.3.5)$$

$$\sigma_{\text{inter}}(\omega, \mu_c, \Gamma, T) \approx i\frac{e^2}{4\pi\hbar} ln\left[\frac{2|\mu_c| - (\omega + i2\Gamma)\hbar}{2|\mu_c| + (\omega + i2\Gamma)\hbar}\right] \quad (2.3.6)$$

In equation (6) kBT is true when it is significantly smaller than both $|\mu c\,|$ and $\hbar\omega$. With controlled voltage $V_{A,}$ when grapheme is external load, its chemical potential μc can be approximated using the following formula.

$$|\mu c| \approx \hbar\, v_F\,(\pi a_0|V_A - V_{Dirac}|)^{\frac{1}{2}} \quad (2.3.7)$$

where the Fermi velocity of the Dirac fermions is approximately v_F = 9 × 105 m/s, the constant determined using a single capacitor model is a_0 ≈ 9 × 1016 m^{-2} V^{-1}, and the Dirac voltage offset induced by natural doping is V_{Dirac} = 0.8V [35].

Intra-band conductivity dominates when the photon energy, ℏω, is less than twice the Fermi energy (2Ef) within the terahertz range. The inter-band conductivity can be neglected under these conditions [35]. This leads to a modified equation:

$$\sigma_{inter}(\omega, \mu c, \Gamma, T) \approx \sigma_{intra}(\omega, \mu c, \Gamma, T) \quad (2.3.8)$$

The surface impedance Zg of graphene is expressed as follows [36]:

$$Zg = \frac{1}{\sigma_g} \quad (2.3.9)$$

where σ_g is the surface conductivity of the graphene.

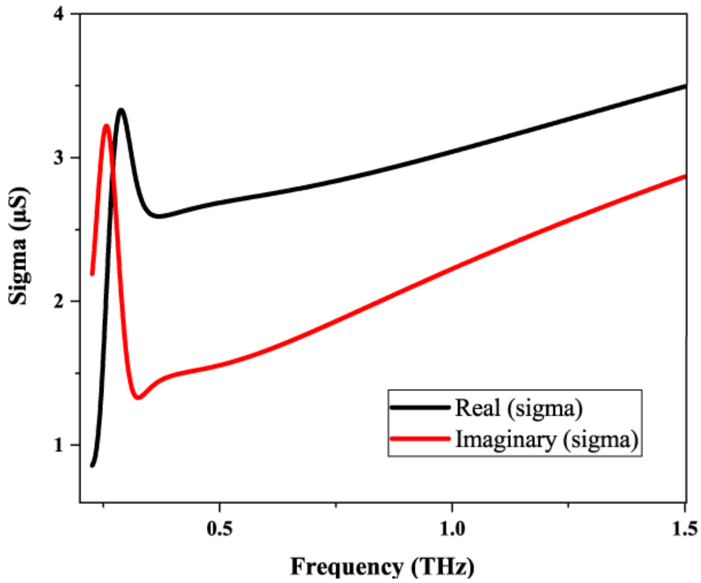

Figure 2.2: Numerical calculations show the real and imaginary parts of the conductance of graphene.

We utilized numerical calculations to determine the real and imaginary components of graphene's surface impedance as, across the studied frequency range, considering a specified relaxation time and temperature as shown in Figure 2.2. For our case, graphene’s chemical potential coincides with a decrease in both the real and imaginary components of surface impedance. It is crucial to highlight the substantial variations in the surface impedance of the graphene layer depending on different values of μ_c. The adjustment of the gate voltage facilitates the alteration of the surface impedance of patterned graphene, thereby influencing the operational efficacy of the proposed GMMA. Consequently, graphene manifests as an optimal material for the fabrication of THz devices, owing to its remarkable tunability. The comprehensive absorbance characteristics of the proposed structure can be elucidated through the effective medium theory [31].

2.4 Equivalent Circuit Model

The theoretical framework underpinning the proposed structure is articulated through the lens of transmission line theory, elaborated upon via its equivalent circuit representation [37]. As illustrated in Figure 2.3, the equivalent circuit of the GMMA is compartmentalized into three distinct impedance section ≈ 377 Ω [38], a value derived from the propagation of THz waves in air. As these waves advance, they encounter the graphene impedance, Zg(f), which in turn engenders an RLC (resistor-inductor-capacitor) resonator within the equivalent circuit. The interaction with graphene impedance significantly influences the overall circuit's behaviour.

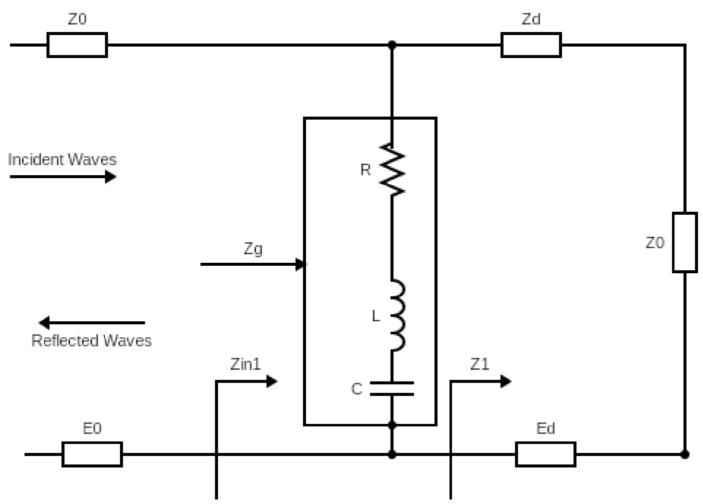

Figure 2.3: Equivalent circuit model of the GMMA, showing intrinsic impedance denoted as Z0, graphene impedance Zg(f),dielectric spacer's impedance Zd, permittivity of free space E0 and permittivity of dielectric Ed respectively.

Subsequently, the dielectric spacer's impedance, akin to that of a short transmission line, is denoted as Zd, dependent on the permittivity of the SiO_2 dielectric material. Given the exceptionally thin nature of the graphene layers compared to THz wavelengths, these layers are effectively modeled as parallel elements within the structure [39]. Referring to Figure 2.3, one can derive the equivalent impedance of the dielectric spacer, contingent upon the dielectric material selected. Additionally, by accounting for graphene's resonance characteristics at specific frequencies, it becomes feasible to integrate a branch in the diagram representing the RLC layer. The subsequent equations provide the calculated values for all impedances illustrated in Figure 2.3 [40].

$$Z_g(f) = R_g(f) + jX_g(f) \tag{2.4.1}$$

$$= R_g(f) + j(2\pi f L_g - \frac{1}{2\pi f C_g});\ Z_g(f) = \frac{1}{\sigma_g} \tag{2.4.2}$$

$$Z_1(f) = jZ_d tan\,(T_1 k_d) \tag{2.4.3}$$

$$k_d(f) = 2\pi f\sqrt{\epsilon_0 \epsilon_d \mu_0} \tag{2.4.4}$$

$$Z_d = \sqrt{\frac{\mu_0}{\epsilon_0 \epsilon_d}} \tag{2.4.5}$$

here, $Z1(f\ )$ represents the input surface impedance and $k_d\ (f\ )$ is the wave number. The electrical length of the structure, denoted as $T_1 k_d$, is equivalent to 0.7192 radians, progressing from the short circuit to the source. As illustrated in Figure 2.3, Zin1(f) is determined by the impedance of graphene (Zg(f)) and the dielectric spacer, which is represented by a short transmission line, as well as the impedances associated with free space (Zd, Z0). This approach determines Zin using the analogous circuit model and demonstrates low signal reflection during the impedance matching condition (Zin=Z0).

2.5 Simulation Results and Analysis

We have performed the simulation using Finite Difference Time Domain - FDTD (Ansys Lumerical software, release 2018 version 8.19.1584.). A 2D model of graphene with conductivity scaling factor of 2 is placed on the top layer of simulation setup. For the fishnet, split ring or rectangular geometry, polygonal object with a refractive index of 1.53, matching the refractive index of background are used to pattern the 2D rectangular graphene sheet. A perfect electrical conductor (PEC) boundary is applied to ‘Z min’ boundary of the simulation region, a perfect mirror and background refractive index of 1.543 is used. Symmetric and antisymmetric boundary conditions are applied along the x and y axis respectively. A broad band plane wave source of bandwidth 1.53 THz and a central frequency of 2.8 THz are used. For each test case, several energy levels of 0 eV, 0.1 eV, 0.2 eV, 0.3 eV, 0.4 eV, and 0.5 eV were used.

2.5.1 Parameter optimization and robustness assessment

We carried out a detailed evaluation of the structural parameters of the proposed metamaterial design to understand how different parameter deviations might affect its performance. The bandwidth deviations for the proposed GMMA are calculated across various parameter ranges: d ranges from 0.1 μm to 1.5 μm, number of split rings ranges from 1 to 4, split size ranges from no split to 40°, and b ranges from 0.5 μm to 1.8 μm. Our primary goal is to maximize the bandwidth for the GMMA structure. The maximum bandwidth 3.8 THz is obtained in the range of 1.1 THz to 4.9 THz with absorption >79% to 95%. The optimized parameters for the GMMA are as follows: d=1μm, number of split rings n=3, split size = 20°, b=1 μm, tg is the thickness of the graphene sheet and ts = 35.9 μm. As our aim is to get the maximum bandwidth, the analyzed data presented in the Table 2.2 is measured starting from absorbance 80% and above, including the maximum absorbance achieved.

Table 2.2: Comparison of different percentages of absorption achieved and their corresponding bandwidths for 4 different test cases.

Sl	Structure	Bandwidth (THz)	Freq Range (THZ)	Absorption	Highest Absorption
1.	Fishnet	2.2	1.7 – 3.9	90%	98%
2.	Fishnet + Circular Split Ring	2.1	2.2 – 4.3	90%	99.7%
3.	Fishnet + Rectangular Split Rings	2.4	1.9 – 4.3	60%	78%
4.	Fishnet+Triple Circular Split Rings	2.9	1.8 – 4.7	90%	94%

Our goal is to achieve the optimal bandwidth performance for our GMMA structure. Given the complex fabrication process of metamaterials, some inaccuracies are unavoidable due to the inherent limitations of the fabrication technology used. We have performed the simulation for 4 different test cases and results are summarized in Figure 2.4.

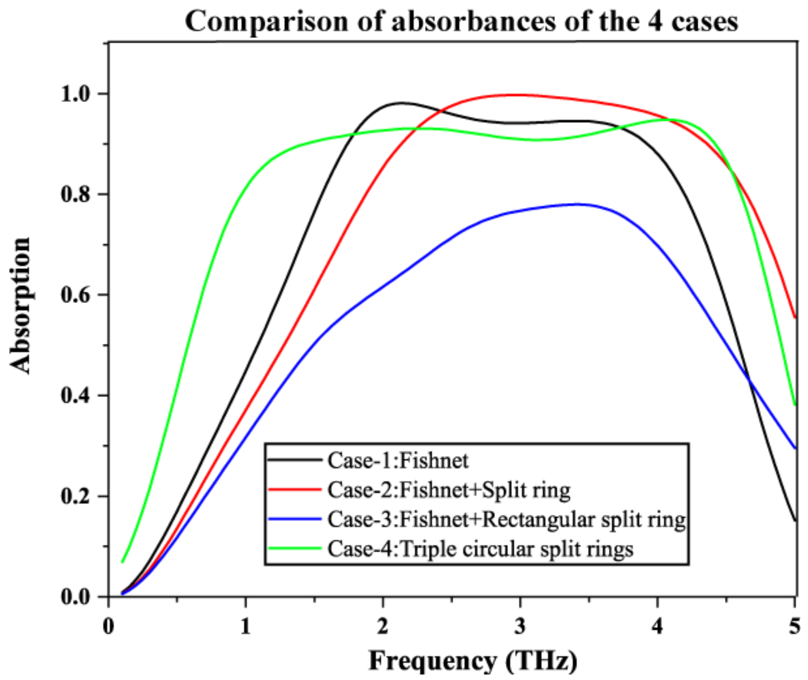

Figure 2.4: Absorption of all 4 cases at 0.5 eV showing different bandwidth for different cases.

The results of Case-1 show very good results in terms of percentage of absorption (efficiency > 95%) with a bandwidth of 2.1 THz at 0.5eV, frequency ranging from 1.88 THz-3.9 THz. The Case-2 shows even better results of absorption, that is, the peak reaches almost 98% and a slightly bigger bandwidth of 2.2 THz, frequency range from 2.1 THz to 4.3 THz. In Case-3, the absorption is >50% and peaks approximately to 80%. However, the bandwidth is quite large, that is, 3 THz ranging 1.5 THZ-4.5 THz. Lastly, in Case-4, where the structure has three split rings shows maximum bandwidth of 3.8 THz with absorption approximately 94%, frequency range 1.1 THz-4.9 THz. All these are the extracted results for 0.5ev. The performance summary of 4 test cases is presented in Table 2.2.

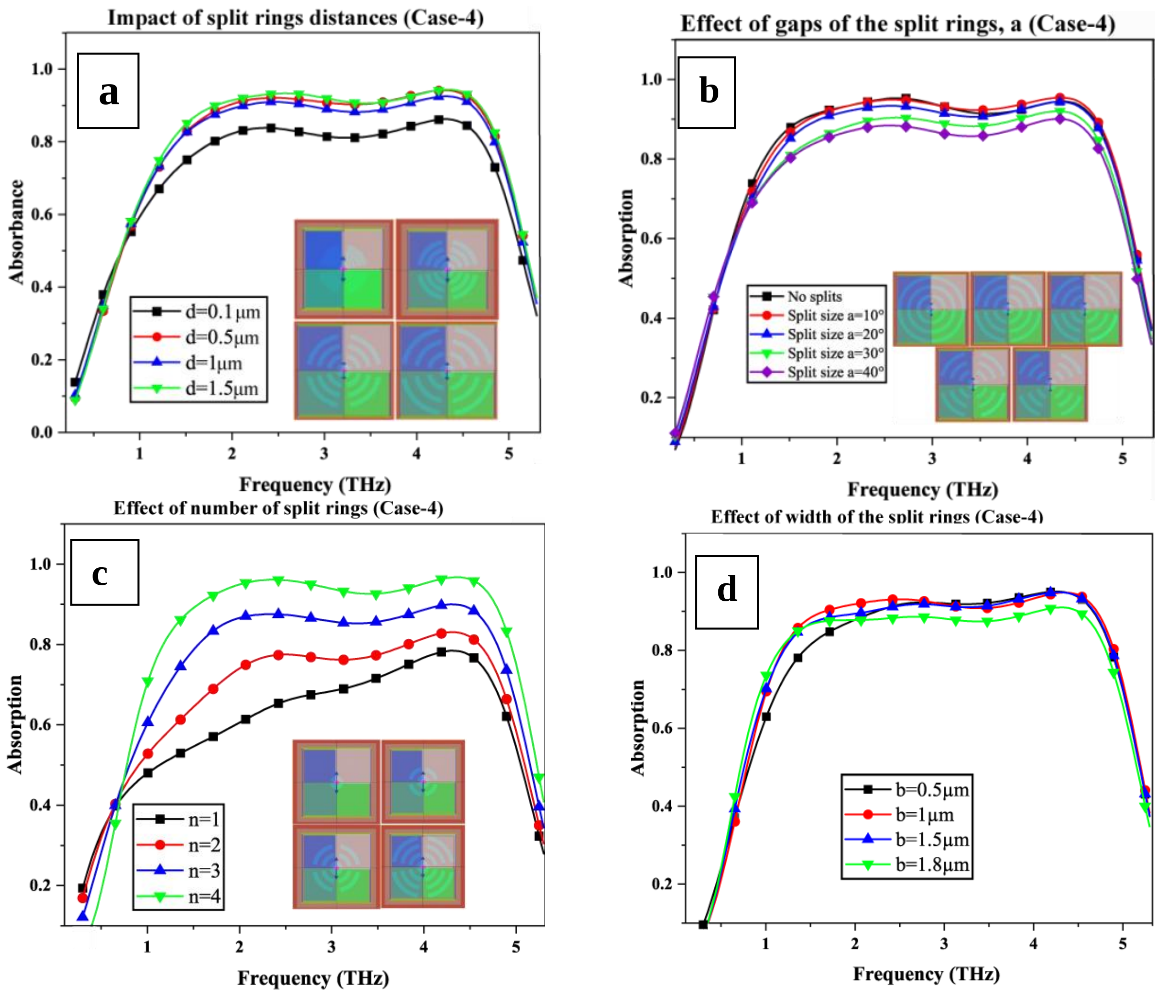

Figure 2.5: Performance analysis of parameter optimization for test case 4 (triple circular split ring). (a) Change of percentage of absorption due to the distances of the split rings from each other, (b) Impact of changes of split size of the rings, (c) Efficiency achieved by changing the number of split rings, (d) Effect of width of the split rings.

The absorption spectrum of the graphene absorber can be tailed by changing the key geometric parameters. To understand the potential impact, some comprehensive assessments have been done for Case-4 by tuning the structural parameters. The percentage of absorption increases with the increase of the distances between 3 split rings but there is no significant change when the distance d is 1.5 μm and above shown in Figure 2.5(a).

Another important structural parameter is the size of the split gaps among all the rings. The split gaps of all the rings are equal. Figure 2.5(b) shows increasing efficiency with the decreasing split sizes of the rings but there is no effect on the bandwidth.

Furthermore, the number of split rings plays a great role in improving the efficiency of the unit cell. From Figure 2.5(c), it is evident that with the increasing number of split rings and its radius, the absorption also increases.

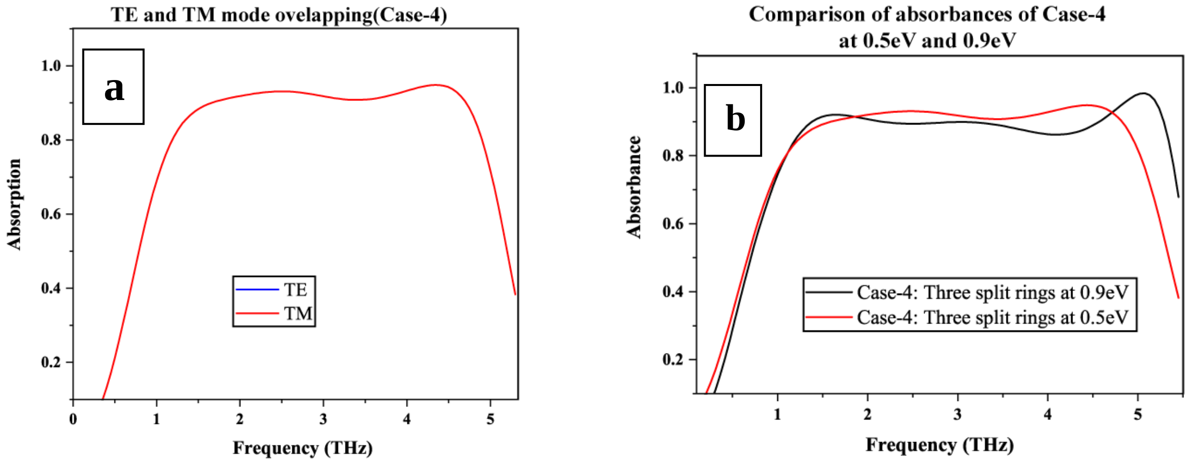

Figure 2.6: (a) Overlapping absorbance spectra for TM and TE mode, (b) Comparison of absorption obtained at 0.5ev and 0.9 eV for the Case-4 only.

The structural parameter b (thickness of the split rings) also affects the efficiency of the cell absorption. The simulation results show that with the increase of the thickness (width) of b, the absorption decreases but the bandwidth increases as shown in Figure 2.5(d). The simulation also was carried out in both TE and TM mode for Case-4 where the efficiency is the same, shown in Figure 2.6 (a). For further investigation, the simulation was carried out for different potentials by adjusting the wavelength and frequency. Figure 2.6 (b) shows a

Table 2.3: Comprehensive study of bandwidth and efficiency with the changes of structural parameters.

Sl	**Structure Parameter**	**Value**	**BW (THz)**	**BW Deviation (%) (Only highest BW at absorption >80%)**	**Max Absorbance**
1	d	0.1 µm	↓	-23.38%	85%
		0.5µm	↓	-10.53%	94%
		1µm(optimized)	3.8	-	94.50%
		1.5µm	↑	+5.2%	95%
2	Number of split rings, n	1	↓	N/A	78%
		2	↓	-71.8%	82%
		3	3.1	-	90%
		4	↑	+15.63%	96%
3	Split size	No splits in the ring	↑	+2.63%	95%
		10°	↑	+5.26%	95%
		20°	3.8	-	93%
		30°	↓	-10.53%	90%
		40°	↓	-13.16%	87%
4	b	0.5 µm	↓	-13.15%	95%
		1 µm	3.8	-	95%
		1.5 µm	↑	+2.63%	94%
		1.8 µm	↓	-5.25%	89%

comparison between the two maximum efficiencies achieved where the efficiency slightly peaked at 98% with an increase in the bandwidth as well. Therefore, this graph also shows that a triple band absorber can be achieved by adjusting the potentials of the cell.

The Table 2.3 presented gives the relationship between the structural parameters and bandwidth and efficiency. This analysis also included an examination of the bandwidth variations across different parameter configurations, as outlined in Table 2.3. To measure these changes, we used the formula:

$$B_{deviation} = \left(\frac{B_{variable} - B_{based}}{B_{based}} \right) \times 100\%$$

Here, B_{based} represents the bandwidth associated with the optimized parameters from the simulation, $B_{variable}$ denotes the bandwidth corresponding to various parameter variations from the simulation, and $B_{deviation}$ quantifies the percentage deviation between the optimized and simulated bandwidths.

2.6 Possible Fabrication Realization

Fabricating a graphene-dielectric-based metamaterial absorber involves issues such as maintaining uniform graphene layers, controlling dielectric layer thickness, and eliminating flaws during transfer procedures. The sensitivity of graphene to environmental conditions such as humidity and temperature can also have an impact on its performance. To address these difficulties, techniques such as chemical vapour deposition (CVD) for high-quality graphene synthesis, atomic layer deposition (ALD) for precise dielectric layering, and cleanroom settings to minimize contamination are required. Additionally, adding a polymer support during graphene transfer, as well as annealing operations, can assist eliminate flaws and improve the material's overall stability and performance.

The fabrication of the proposed device involves a multi-step process, depicted in Figure 2.7, primarily utilizing the chemical vapour deposition technique, known for its cost-effectiveness and reliability. The primary material in this process is graphene, a single layer of carbon atoms arranged in a hexagonal lattice structure, selected for its exceptional properties. Initially, high-quality monolayer graphene is grown on a copper or nickel substrate using the CVD technique.

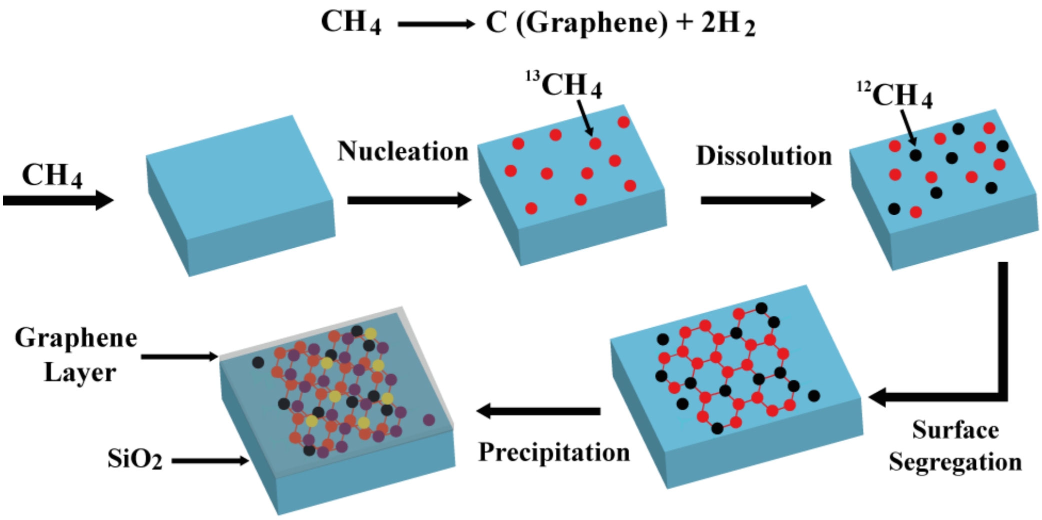

Figure 2.7: Fabrication process of GMMA [41].

This step is crucial for producing a pristine graphene layer, essential for the device's performance. The selection of copper or nickel as substrates provides an appropriate surface for graphene growth while maintaining cost-efficiency. After the graphene layer is grown, it is transferred onto the dielectric material, specifically SiO_2. The production method's flexibility is further enhanced by the capability to transfer CVD-grown graphene to various other substrates [41], allowing for modifications based on specific substrate preferences or application requirements. Spin coating is employed to deposit a thin dielectric layer over the structure following the graphene transfer. This technique ensures uniform distribution of the dielectric material, which is subsequently cured in a vacuum oven. The curing process fortifies the dielectric layer, providing a robust foundation for subsequent graphene layers. The CVD process is repeated for the next graphene layer, wherein a new graphene sheet is grown on a copper substrate and then transferred onto the existing structure. Following this, the dielectric layer is applied to the newly formed graphene sheet using spin coating and cured in a vacuum oven. This stacking process guarantees the development of a strong and efficient device structure. In the final stage of the manufacturing process, conventional lithography is employed to create the top graphene pattern. This comprehensive production process illustrates the strategic integration of materials and techniques to achieve optimal performance, laying the foundation for the successful fabrication of the proposed device. The fabrication of metamaterials has encountered several challenges, such as limited pattern design options, inflexibility in design, difficulties in material selection, uncontrollability, and issues with long range disorder. Key challenges in the practical fabrication of metamaterials include creating three-dimensional structures and producing them on a large scale [42].

2.7 Results and Discussion

This study introduces a graphene-structured metamaterial absorber, which achieves a broadband spectrum with a bandwidth of approximately 3.8 THz, attaining over 95% efficiency from 1.1 THz to 4.9 THz. Subsequently, this structure was fine-tuned to various other geometric configurations to achieve improved bandwidth and absorption. The simulation carried out for 0eV, 0.1 eV, 0.2 eV, 0.3 eV and 0.5 eV. The GMMA displays several remarkable features such as tunability, polarization independence, and robustness against structural changes. Further optimization of the aforementioned structure can lead to even better results. One crucial factor contributing to increased absorption is the addition of circular structures onto the fishnet. As the number of circular structures increases, absorption percentage also rises significantly, reaching close to 97% sweeping from 0.5 eV to 0.8eV but slightly drops at 0.9eV.

Table 2.4: Comparison of bandwidth across different GMMA configurations.

Sl	References	Year	Constituent material	Bandwidth over 90% (THz)	Maximum Absorption
1.	Lie et al.[43]	2015	Graphene,SiO_2, and gold	1.22	>90%
2.	R. Gao et. al. [44]	2015	Graphene, silicon, dielectric	0.14	99.8%
3.	Liu W. et. al [45]	2021	Gold, graphene, dielectric	3.26	98.21%
4.	H. Yu et al. [46]	2021	Graphene, SiO_2, gold	0.931	>95%
5.	B Xiao et al. [47]	2017	SiO_2, gold, graphene	2.85	>90%
6.	A. Beheshti et al. [48]	2021	Gold, graphene, SiO_2	1	95%
7.	S.K. Patel et al. [49]	2019	Graphene, silver, SiO_2, gold	In wide different ranges of 100 to 1600	Average 85.48% in infrared, 97.51% in visible, 89.57% in the ultraviolet region
8.	This study	2024	Graphene, metal, dielectric	3.8	95%

We have also compared our findings with available literature as summarised in Table 2.4.We have selected the graphene based metamaterial and found BW over 90% varies from 0.14 2.85THz. Our findings outperformed the reported literature and showed 1.5 times higher BW compared to report highest BW.

In a recent study, Ben Xin Wang et al. [50] presented a terahertz metamaterial (Aluminium and polyamide) consists of U-shaped split-ring resonator and a fork-shaped resonator that can demonstrate a triple-band electromagnetically induced transparency (EIT) effect, by coupling two "big-bright" modes. Three transparency peaks around 0.59 THz, 1.07 THz, and 1.34 THz, bandwidth of three peaks was around 0.1 THZ and maximum transmission peaks within 50-75% are experimentally realized, and their formation mechanisms were explored.

Jia-Hao Deng et al. [51] proposes a metasurface based microwave power detector based on a metal resonant disk and load resistors for detecting the polarization angle of microwave signals. The simulation and experimental verification demonstrate that the detector exhibits high absorption efficiency, wide detection angle, and polarization insensitivity providing a potential solution for large area microwave power detection.

In a recent review, Ben Xin Wang et al. [52] emphasizes the importance of dielectric based metamaterial absorber (DBMAs)as metallic metamaterial absorber poses many unfavourable challenges such as non adjustable absorption, easy oxidation, low melting, and expensive preparation cost. Different types of theories and physical mechanisms such as Mie resonance, guided mode resonance, and anapole resonance also confirm the near perfect absorption of such DBMAs for various applications (stealth technology, solar energy absorption and electromagnetic interference suppression).

From the above analysis we can confirm that the proposed graphene-metal-dielectric based absorber outperformed the reported literature demonstrating excellent performances such as BW around 3.8 THz, maximum absorption around 95%, within a broad frequency range of 1.5-4 THz, irrespective of polarization. Though the experimental verification is beyond the scope of this study however the simulation's findings was verified using transmission line theory analyzing relationship between input impedance and reflection coefficient.

The novelty of this proposed structure is that GMMA exhibits several noteworthy characteristics, including tunability, polarization insensitivity, and resilience to variations in structure, making it suitable for various applications in the terahertz spectrum. The demonstrated tunable and wide bandwidth capabilities represent significant advancements in GMMA technology tailored for terahertz frequencies. Moreover, it's simple design renders it might be suitable for stealth technology, solar energy absorption, thermophotovoltaic systems for energy production, antenna design and electromagnetic interference suppression. Overall, the versatility and adaptability of GMMA position it as a valuable solution for addressing challenges and requirements in pioneering terahertz innovations. This research not only propels the progress of the technology but also opens up new avenues for practical implementations.

2.8 Conclusion

We have introduced an innovative design for a graphene based metamaterial absorber that exhibits the ability to absorb over 90% of EM waves across a broad frequency range (1.1-4.9 THz), irrespective of polarization. The findings of the study were also verified by equivalent circuit model. The GMMA displays several remarkable features such as tunability, polarization independence, and robustness against structural changes. These characteristics make the GMMA an excellent contender for various applications within the THz range. The tunable and broadband capabilities demonstrated in this study significantly enhance the development of GMMA technology specifically designed for THz frequencies. Furthermore, the GMMA’s versatility and adaptability position it as a valuable tool in addressing the challenges and requirements of pioneering innovations in the THz spectrum. This research not only contributes to the advancement of GMMA technology but also opens up new possibilities for its practical applications. To sum up, the structure’s exceptional clarity and simplicity make it ideally suited for several applications such as stealth technology, solar energy absorption, THz imaging and sensing and antenna applications.

Chapter 3

Graphene PCM Metamaterial (GPCM) Based Wideband Tunable THz Absorber Using Fishnet and Circular Split Ring Structure

3.1 Introduction

In this study we investigated a novel approach to designing a graphene metamaterial based terahertz absorber with dual-mode functionality, tunability, and broadband absorption capabilities. The study leverages the unique properties of graphene, a material known for its exceptional electronic and optical characteristics, combined with metamaterials to achieve efficient THz absorption. Here we performed extensive simulation on five different types of configurations and found the optimized structure with phase change material vanadium dioxide (VO_2) has the highest bandwidth of 7.69 THz and absorption over 90%. The tunability of the absorber is a significant feature, allowing for dynamic adjustment of the absorption frequency, which is crucial for applications in THz imaging, sensing, and communication systems. The broadband nature of the absorber ensures effective performance over a wide range of frequencies, addressing the need for flexible and high-performance devices in emerging THz technologies. This work represents a significant advancement in the field of THz metamaterials, with potential implications for the development of next-generation THz devices. Spectral selective absorption filters are made possible by resonant absorbers based on plasmonic materials, metamaterials, and thin filters, where absorption is highest at the resonance wavelength. Resonant absorbers are made to function at a variety of wavelengths for use in thermal emitters, thermovoltaic devices, sensors, absorption filters and other applications by adjusting the geometrical parameters of nano or microstructures and refractive indices of materials. The spectral absorption response is difficult to control and tune after resonant absorbers are constructed. Materials that undergo phase change, like VO_2, used as metal in this study, offer practical ways to modify optical characteristics in relation to temperature.

3.2 Literature Review

In recent years, there has been significant progress in development of sub-wavelength micro-nano structure with extraordinary optical properties, including metasurface and metamaterials. This progress has been fuelled by the introduction of conductive materials with tunable optical characteristics, such as graphene, vanadium dioxide and semiconductors. These structures allow for the manipulation of electromagnetic waves at sub-wavelength scales, resulting in unique electromagnetic properties like negative refractive index, super focusing, and optical stealth. These conductive materials can adjust their characteristics in response to external influence like temperature, electric fields and light. This versatility allows for modifications in the amplitude, phase, polarization and direction of electromagnetic waves.

The idea of a 'perfect absorber' capable of nearly 100% absorption within a specific frequency range, was first introduced in 2008 [6]. By integrating metamaterials with the adjustable characteristics of liquid crystal materials, electronically tunable metamaterial absorbers can be developed. Recently, graphene, a two-dimensional material known for its exceptional optical properties, has been incorporated into metamaterials. Graphene's distinct single-atomic layer structure provides superior optical conductivity and great carrier mobility. In parallel, graphene's carbon atoms create bonds with sp2 hybridization orbital, which allow graphene to sustain surface plasmon resonance (SPs). As a result, graphene has the ability to both absorb and transmit electromagnetic waves. Furthermore, we can dynamically modify absorption peaks without sacrificing absorption efficiency by actively modulating graphene's Fermi energy by the application of an external bias voltage [53]. This makes graphene based metamaterials ideal for designing tunable absorbers. Graphene has optical characteristics that are similar to those of a Drude-type material at lower frequencies. These substances encourage the development of surface Plasmon polarities (SPP). The collective oscillation of light and the charge density at the interface between a graphene sheet and its surroundings is known as an SPP [54]. Like other waves (sound or light), an SPP supported at a graphene contact can be steered in a variety of ways. The metamaterial and plasmonic communities were particularly interested in this characteristic [55]. The use of graphene in the optical domain may lead to a wide range of applications, from transformation optics and graphene-based optical modulators [56] to many other devices. Examples of the adaptability of graphene have previously been shown experimentally and supported by strong evidence [57].

Of particular interest among these materials is VO_2 which exhibits a phase transition from an insulator to a metal. This insulator-metal transition (IMT) in VO_2 occurs when it reaches its phase transition temperature, changing its crystal structure from monoclinic to rutile. This phase shift can be triggered by thermal, electrical [58] or optical and thermal properties. These properties make VO_2 well-suited for developing tunable optical devices, including nano-antennas, modulators and tunable polarizers.

VO_2 was first discovered by Morin in 1959 [59]. When the temperature drops below 68°C ($T_c \approx$ 340 K), VO_2 undergoes a metal-insulator transition (MIT), changing its crystal structure from rutile to monoclinic. Under standard pressure, VO_2 takes on a tetragonal rutile (R) structure and adopts a monoclinic. At temperature below $\tau_c = 68°$ C, VO_2 transitions from a metallic state to an insulating state [60]. This metal-insulator transition (MIT) brings about substantial changes in vanadium dioxide's optical constants, crystal structure, lattice parameters, and electrical conductivity. This transition can be initiated through temperature changes, current application, or light exposure, enabling VO_2 to dynamically control electromagnetic waves. It is not uncommon to witness a resistivity change exceeding four orders of magnitude as the temperature is cycled through the phase transition of VO_2. With a bandgap energy ranging from 0.6 to 0.7 eV, the semiconductor phase exhibits substantial infrared transmittance [61]. Optical and resistivity measurements of VO_2 thin film display hysteresis shows the potential use in thermally activated electronic or optical switching devices. Numerous studies have explored its various applications, including erasable optical storage systems based on VO_2. Given the extreme sensitivity of terahertz signals to conductivity, the dramatic change in conductivity triggered by the phase change in VO_2, makes it a valuable component for metamaterials [62]. Integrating phase-change functionality with metamaterials represents a promising direction, enabling the development of high-contrast, electrically or optically controlled metamaterial devices. Compared to other phase-change material VO_2, exhibits an exceptionally large shift in conductivity during its phase transition. Moreover, when the phase change is optically induced, response time can be as rapid as picoseconds [62].

With these significant progresses on phase change material, VO_2 has its applications in multiple fields. VO_2-coated smart windows can change from transparent to reflective depending on the external temperature, providing energy-efficient control over sunlight and heat entering a building [63]. In infrared sensors and optical modulators, VO_2's phase transition properties are leveraged to control light absorption and reflection dynamically [59]. Again, in infrared sensors and optical modulators, the phase transition properties are leveraged to control light absorption and reflection dramatically [64]. Most importantly, vanadium dioxide’s fast-switching capabilities and tunable electrical conductivity make it valuable in radio frequency (RF) and microwave application [65].

3.3 Structural Design and Methodology

In this chapter, we investigated the resonator shapes to get a better absorption bandwidth compared to the structures in the previous chapter. The basic design architecture is the same as 3-layered using graphene, dielectric and metal. We used the phase change material crystalline VO_2, graphene sheet and silicon dioxide. Initially, we started with 4 circular split rings of resonant structures (Figure 3.1a) and found out the best suitable split gap and ring thickness.

Secondly, we replaced the innermost circular split ring with a cross-shaped (Figure 3.1b) to understand the resonant effect comparing between circular and rectangular structures. This way we reached the fifth structure explained in Figure 3.1. The five different structures are described below.

3.3.1. Case-1: Four Circular Split Rings

The Figure 3.1(a) is the structure of the first case absorber where only the top unit is shown. There are 4 circular split rings of four different radii. All the ring structures are of equal width b=1 µm and placed apart in equal distances d=1 µm. The four of the rings have 4 splits of gap size *a*=10°. Other structural parameters are: P=18 µm, outer radius r1=1.5 µm, outer radius r2=3.5 µm, outer radius r3= 5.5 µm, outer radius r4=7.5 µm.

3.3.2. Case-2: Three Circular Split Ring + Cross

With the exception of introduction of a cross-structure in place of the initial ring, this construction is nearly identical to Case-1. The refractive indices are similar to Case-1 as well. The dimension of the rectangular split structures are the same as that of Case-1 as shown in Figure 3.1 (b). The structural parameters are as follows: P=18 µm, outer radius r1=3.5 µm, outer radius r2= 5.5 µm, outer radius r3=7.5 µm, splits of gap size *a*=10° and the thickness of the split rings b=1 µm. The length of the cross-shape is equal to its width c=3.5 µm and its thickness is *w*=0.7 µm.

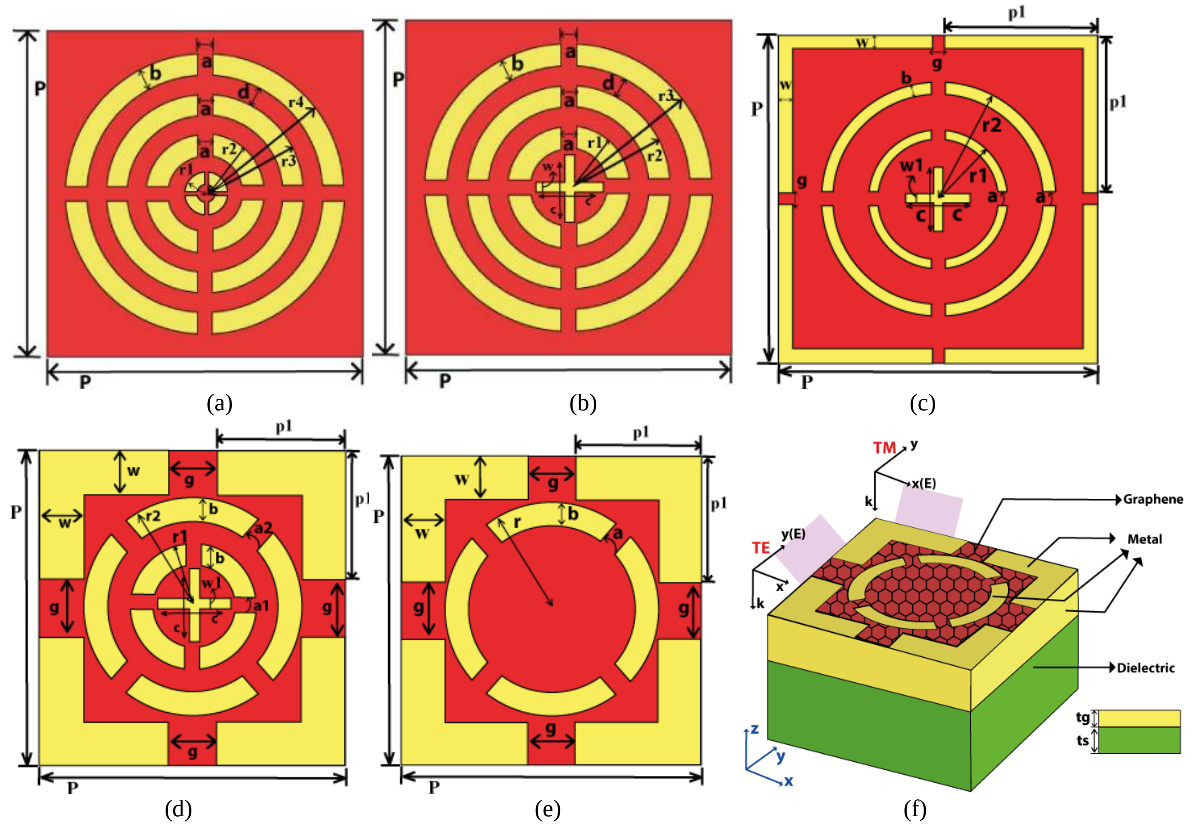

Figure 3.1: (a) Top view of the structure in Case-1 (4-Circular Rings), (b) Top view of the structure in Case-2 (3-Split Rings+Cross), (c) Top view of the structure in Case-3 (Fishnet+2-Split Rings+Cross) where the thickness of all the structures are thinner than the other cases, (d) Top view of the structure in Case-4 (Fishnet+Circular Maze+Cross), (e) Top view of the structure in Case-5 (Fishnet+ Split Ring), (f) Perspective 3D view of the structure in Case-5, side view (x,z) of all the unit cell; t_g *and* t_s*. Green=*SO_2 *and Yellow=* VO_2.

3.3.3. Case-3: Fishnet + Two Circular Split Ring + Cross

As seen in Figure 3.1 (c), the top unit of this structure is made up of thinner resonant structures. It includes a cross-structure in the centre, two circular split rings, and an outer rectangular split ring. These structures are narrower in this instance to maintain greater gaps of distance 2 µm. The dimension of the top cell is as follows: P=18 µm, P1=7 µm, g=1µm, *w*=0.5 µm, outer radius r1=3.5 µm, outer radius r2=6.5 µm. The thickness of the split rings b=1 µm and they have equal gap sizes *a*=10°. The length and width of the cross-shape in the middle is the same i.e. c=4 µm and has thickness w1=1 µm.

3.3.4. Case-4: Fishnet + Maze + Cross

Case-4's structure is identical to Case-3's structure, but as Figure 3.1 (d) illustrates, they are thicker and closer to one another. The circular maze like construction, consisting of two circular split rings spaced 1 µm apart has the following dimension: outer radius r1=3 µm, outer r2=5 µm, split gap size of the first ring a1=20°, split size of the second ring a2=20°, and thickness b=1 µm. The following are the further structural parameters: *w*=1.5 µm, P=18 µm and p1=6 µm. The dimensions of the cross-shape are c=3 µm for both length and width, and w1=0.5 µm for thickness.

3.3.5. Case-5: Fishnet + Circular Split Ring

The top view and the 3D view of the structure of Case-5 is shown in Figure 3.1 (e) and (f) respectively. The sole optimization to the top unit cell is that the cross-shape and a ring have been removed. This is the final optimized structure chosen has the following measurements: p1=6 µm, thickness of the rectangular ring *w*=1.5 µm, gap g=1 µm, P=16 µm, outer radius r=5 µm, split gap size of the ring *a*=10°, thickness of the circular ring b=1 µm.

The proposed structure shown in Figure 3.1 (f) illustrates the 3D and top view of the cell of Graphene Metamaterial Absorber. The structures presented in Figure 3.1 show the steps of investigating the absorption by manipulating the resonant structure and their material. This absorber comprises three layers: the upper layer is designed; the middle layer is the dielectric consisting of the phase change material VO_2 around it. The bottom layer is the SiO_2 with refractive index 1.43 micrometers. The SiO_2 demonstrates minimal dielectric dispersion, ensuring a consistent dielectric constant across various frequencies. The thickness of the VO_2 and SiO_2 layers is represented by t_g and t_s, respectively, as shown in Figure 3.1 (f).

To model electromagnetic (EM) behaviour accurately, open boundary conditions are applied to the simulations. Periodic boundary conditions in the z-direction simulate infinite space, while in the x and y directions, they enable the periodic repetition of the simulation unit. These boundary conditions work together to provide a detailed representation of EM interactions,

Table 3.1: Dimensions of the cells and the resonant structures of the proposed 5 structures.

Sl	Structure Parameter	Case 1: Split Rings (µm) (fig.3.1a)	Case 2: Split Rings+Cross (µm) (fig.3.1b)	Case 3: Fishnet+Split Rings+Cross (µm) (fig.3.1c)	Case 4: Fishnet+Maze + Cross (µm) (fig.3.1d)	Case 5: Fishnet+Split Ring (µm) (fig.3.1e)
1	Top side layer (VO_2 as metal)	Length(P) =18, Width(P) =18, Outer radius r1=1.5, r2=3.5, r3= 5.5, r4=7.5, Split gap *a*=10° Thickness b=1, Height=1	Length(P)=18, Width(P)=18 , Outer Radius r1=3.5, r2= 5.5, r3=7.5, Thickness b=1, Split gap *a*=10° Length & Width of Cross-sign c = 3.5, Height=1	Length(P)= 18, Width(P)=18, Split gap g=1, Thickness *w*=0.5, Outer Radius r1=3.5, r2=6.5, Split gap *a*=10° Thickness b =1, Cross-sign c = 4.5, Thickness w1= 0.5, Height=1	Length(P)= 18, Width(P)=18, Split gap g=2, Thickness *w* =1.5, Outer radius r1=3, r2= 5, Ring split sizes a1=20°, a2=20°, Thickness b=1, Length & Width of Cross-sign c=4, Thickness b=1, Height =1	Length(P) = 16, Width (P) = 16, Split gap g=2, Outer radius r= 5, Ring split sizes *a*=10°, Thickness b=1, Height H =1
2	Top middle layer (2D graphene sheet)	Length= 20 Width= 20	Length=20 Width=20	Length =20 Width =20	Length =20 Width =20	Length =18 µm Width =18 µm
3	Bottom layer (SiO_2)	Length= 18 Width= 18 Height t_s=35.9	Length =18 Width = 18 Height t_s =35.9	Length =18 Width = 18 Height t_s =35.9	Length =18 Width = 18 Height t_s =35.9	Length =16 Width =16 Height t_s =16

improving the precision of the simulation results. The research focuses on the detailed behaviour of the transverse electric (TE) waves, oriented perpendicular to the propagation axis.

The analysis is conducted in the x-z incident plane, with special attention to the azimuthal angle φ set at θ°, defining the TE wave's orientation within the *x-y* axis.

We used numerical calculations to determine the real and imaginary parts of graphene's surface impedance over the studied frequency range, taking into account a special relaxation time and temperature, as shown in Figure 3.2(a). In this instance, a drop in the real and imaginary components of the surface impedance is correlated with graphene's chemical potential. Notably, the surface impedance of the graphene layer varies significantly with different values of μc. Adjusting the gate voltage allows for tuning the surface impedance of patterned graphene, thereby impacting the performance of the proposed GMMA. As a result, graphene stands out as an ideal material for THz device fabrication due to its exceptional tenability. The comprehensive absorbance properties of the proposed structure can be explained using effective medium theory [66].

While the other states of VO_2 remain constant even after the stimulus has been removed, the phase of VO_2 is solely dependent on whether the external stimulus is provided or not. This makes it possible to regulate the VO_2 phase only by temperature rather than requiring quick heating or cooling to alter its state. While the imaginary part of the refractive index or absorption increases dramatically at near infrared wavelength, its properties in the visible regime remain largely unchanged as it transitions from an insulating phase at low temperatures to a metallic phase at higher temperatures. Trevon et al. [67] introduced the process of collecting VO_2 samples in both metal and insulator forms. In this study, VO2 sample data as the metal has been implemented. The sputtering technique was used to create the VO2 film samples, which were then annealed. A temperature controlled ellipsometer was used to test their temperature dependent refractive index. The measured refractive indices are shown in Figure 3.2(b).

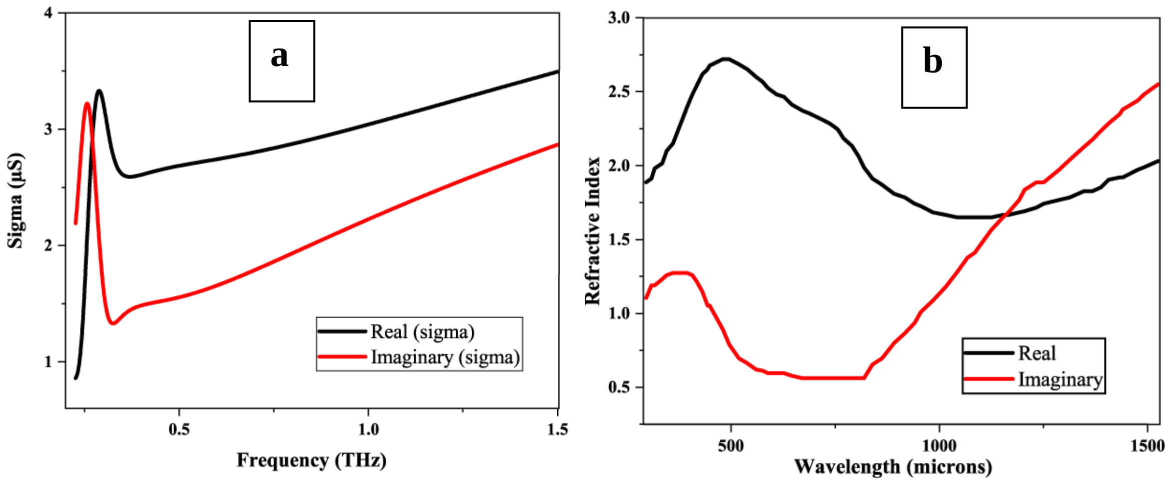

Figure 3.2: (a) Numerical calculations show the real and imaginary parts of the conductance of graphene, (b) Refractive index of vanadium dioxide as a metal.

The simulation was performed using Finite Difference Time Domain - FDTD (Ansys Lumerical software, release 2018 version 8.19.1584.). A 2D model of graphene with conductivity scaling factor of 2 is placed on the top layer of simulation setup. For the fishnet, split ring or rectangular geometry, polygonal objects with a refractive index of 1.53, matching the refractive index of background are used to pattern the 2D rectangular graphene sheet. In the 'source' settings, a slight long pulse has been used that minimizes the numerical stability problem. The selected source setting is plane wave broadband, of central frequency 6 THz with a bandwidth of 10 THz. A perfect electrical conductor (PEC) boundary is applied to 'Z min' boundary of the simulation region, a perfect mirror and background refractive index of 1.543 is used. Symmetric and antisymmetric boundary conditions are applied along the x and y axis respectively. For each test case, several energy levels of 0.2 eV, 0.3 eV, 0.4 eV, and 0.5 eV were used.

3.4 Theoretical Analysis and Equivalent Circuit Model

The absorption coefficient (A) for the proposed structure was computed using the formula,

$$A = 1 - |S_{21}|^2 - |S_{11}|^2 \tag{3.4.1}$$
$$= 1 - |S_{11}|^2$$
$$= 1 - R$$

where transmission (S_{21}) (also called T) and reflection $R = S_{11}$.

The permittivity of phase change material is described by the Drude model with other summands. The model dielectric function ε(ω) used is made up of the following: (1) a constant that explains the polarizability in the higher range, such as, the core electron contribution (2) a Drude-type contribution for free the crystalline samples' carriers and lastly, (3) a Tauc-Lorentz oscillator to explain how optical transitions be [68] :

$$\varepsilon(\omega) = \varepsilon_{const} + \varepsilon_{Drude} + \varepsilon_{Tauc-Lorentz}(\omega)$$

$$\varepsilon_{Drude} = \frac{\omega_p^2}{\omega(\omega + iy)}$$

$$Im\big(\varepsilon_{Tauc-Lorentz}(\omega)\big) = \frac{1}{\omega}\,\frac{S^2\omega_0\gamma(\omega - \omega_{gap})}{\omega(\omega^2 - \omega_0^2)^2 + \omega^2\gamma^2}\;\;\Theta(\omega - \omega_{gap})$$

The permittivity of graphene (ε_g) can be expressed by the following equation [34]:

$$\varepsilon_g = 1 + j\frac{\sigma(\omega)}{\varepsilon_0 \omega t_g} \tag{3.4.2}$$

where, ω = angular frequency

t_g = thickness of graphene layer

ε_0 = permittivity in vacuum

$\sigma(\omega)$ = complex surface conductivity of graphene

The surface conductivity of graphene $\sigma(\omega)$ is typically a combination of intra-band conductivity and inter-band conductivity. In the terahertz to optical frequency range, the complex surface conductivity $\sigma(\omega)$ of graphene can be characterized by Kubo formula [35]:

$$(\omega, \mu_c, \Gamma, T) = \sigma_{\text{intra}}(\omega, \mu_c, \Gamma, T) + \sigma_{\text{inter}}(\omega, \mu_c, \Gamma, T)$$

$$= -\frac{ie2kBT}{\pi\hbar^2}\left[\frac{1}{(\omega+i2\Gamma)^2}\int_0^\infty d\epsilon\left(\frac{\delta n_F(\epsilon)}{\delta_\epsilon} - \frac{\delta n_F(-\epsilon)}{\delta_\epsilon}\right)\epsilon - \int_0^\infty d\epsilon\,\frac{n_F(-\epsilon)-n_F(\epsilon)}{(\omega+i2\Gamma)^2-4(\frac{\epsilon}{\hbar})^2}\right] \quad (3.4.3)$$

where, σ_{intra} and σ_{inter} respectively stand for intra-band and inter-band conductivities. Here ϵ refers to the energy of the charge carriers of electrons and ω represents the radian frequency in wave-related context. In the terahertz range, intra-band conductivity is dominant when the photon energy, $\hbar\omega$, is less than twice the Fermi energy ($2E_f$). In these circumstances, the inter-band conductivity can be disregarded [35]. As a result, the equation is altered.

$$\sigma_{inter}(\omega, \mu_c, \Gamma, T) \approx \sigma_{intra}(\omega, \mu_c, \Gamma, T) \quad (3.4.4)$$

The surface impedance Z_g of graphene is expressed as follows [36]:

$$Z_g = \frac{1}{\sigma_g} \quad (3.4.55)$$

where σ_g is the surface conductivity of graphene.

Transmission line theory serves as the theoretical foundation for the suggested structure and it is further developed by its equivalent circuit representation [37]. Three separate impedance sections ≈ 377Ω [38], which are based on the propagation of THz waves in the air, make up the equivalent circuit of the GMMA, as shown in Figure 3.3. The graphene impedance $Z_g(f)$, is encountered by these waves as they progress, creating an RLC (resistor-inductor-capacitor) resonator in the equivalent circuit. The behaviour of the entire circuit is greatly influenced by the contact with graphene impedance. Then, the permittivity of the SiO_2 dielectric material determines the dielectric spacer's impedance, which is represented by Zd and is similar to that of a short transmission line.

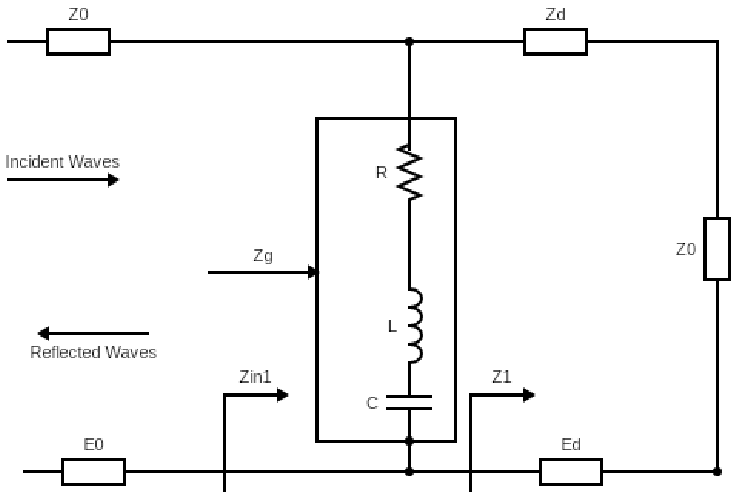

Figure 3.3: Equivalent circuit model of the GMMA, showing intrinsic impedance denoted as Z0, graphene impedance Zg, dielectric spacer's impedance Zd, permittivity of free space E0 and permittivity of dielectric Ed respectively.

Since the graphene layers are quite thin in comparison to THz wavelengths, they can be efficiently represented as parallel components in the source [39]. Depending on the dielectric material chosen, the equivalent impedance of the dielectric spacer can be calculated using Figure 3.3. Furthermore, it is possible to incorporate a branch in the Figure 3.3 that depicts the RLC layer by taking into consideration the resonance properties of graphene at particular frequencies. The computed values for each of the impedances shown in Figure 3.3 are given by the following equations [40].

$$Z_g(f) = R_g(f) + jX_g(f) \tag{3.4.6}$$

$$= R_g(f) + j(2\pi f L_g - \frac{1}{2\pi f C_g}); \qquad Z_g(f) = \frac{1}{\sigma_g} \tag{3.4.7}$$

$$Z_1(f) = jZ_d \tan{(T_1 k_d)} \tag{3.4.8}$$

$$k_d(f) = 2\pi f\sqrt{\epsilon_0 \epsilon_d \mu_0} \tag{3.4.9}$$

$$Z_d = \sqrt{\frac{\mu_0}{\epsilon_0 \epsilon_d}} \tag{3.4.10}$$

In this case, $k_d(f)$ is the wave number and $Z_1(f)$ is the output surface impedance. Moving from the short circuit to the source, the structure's electrical length, represented by $T_1 k_d$, is equal to 0.7192 radians. Figure 3.3 shows that Zin1(f) is influenced by the graphene impedance

Zg(f), the dielectric spacer (shown by a short transmission line) and the free spacer impedances (Zd,Z0). This method shows little signal reflection during the impedance matching condition (Zin=Z0) and calculates Zin using the analogous circuit model.

3.5 Simulation Results and Analysis

We carried out a comprehensive evaluation of the structural parameters of the proposed metamaterial design to assess how deviations in these parameters influence performance. The bandwidth deviations for the proposed GMMA calculated over different structural parameter ranges: number of circular split rings, rectangular ring split gap *g*, split gap of circular ring *a*, the thickness of the circular ring *b* and the thickness of the rectangular ring *w*. Overall dimension of the optimized cell is 16×16×16 micrometers. The structural dimension of all the 5 cases is presented in Table 3.1 above.

3.5.1 Parameter optimization and robustness assessment

With the help of evaluation results of the previous section, we conducted investigation of the structural parameters of the proposed metamaterial design to further achieve higher absorption bandwidth. The frequency bandwidth and maximum absorption deviations for the proposed graphene metamaterial absorber are calculated across various parameters. These are: number of circular split rings, the thickness of circular and rectangular split rings, split gaps between the rings and their orientation. The maximum absorption and the bandwidth are dependent on these parameters. To verify this, some more simulations were done varying the resonant structures only in Case-5.

With the radius and the thickness of the circular ring unchanged, the gap of the rectangular ring *g* (Figure 3.4 a) was adjusted from 1µm to 4 µm. As shown in Figure 3.4 (a), both absorption and bandwidth decrease as the gap increases, with the best frequency bandwidth achieved at g = 1 µm. When the fishnet structure is kept constant, varying the ring gap *a*, from 10° to 40°, causes the bandwidth to shrink shown in Figure 3.4 (b). If both parameters *g* and *a* are varied together, absorption drops significantly, as depicted in Figure 3.4 (c). In this case, *g* is varied from 1μm to 4μm and *a* is varied from 10° to 40°. Lastly, the impact of the ring thickness *b* and the rectangular thickness w is shown in Figure 3.4 (d). The best bandwidth and absorption were observed with *w*=1 μm and *a*=10°. Reducing the thickness causes a drop in absorption, while increasing the thickness reduces absorption in higher frequencies, affecting the bandwidth.

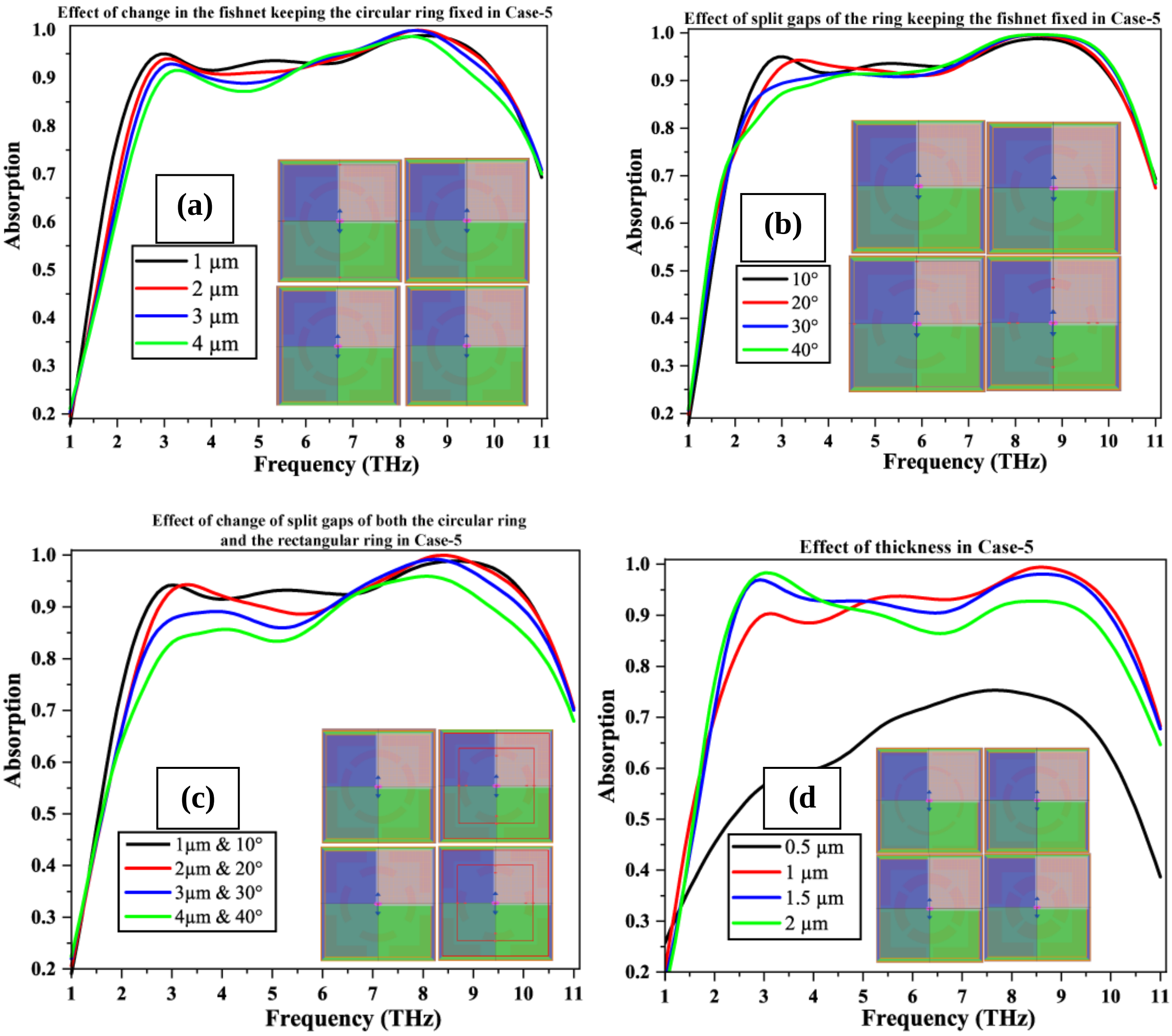

Figure 3.4: Performance analysis of parameter optimization for test case 5 (Fishnet + Split Ring). (a) Change of percentage of absorption due to the change in the fishnet, keeping the circular ring unchanged, (b) Impact of changes of split size of the rings, keeping the fishnet fixed, (c) Absorption achieved by changing both fishnet and the split ring gaps, (d) Effect of thickness of all the resonant structures.

Our primary goal is to achieve the optimal bandwidth performance for our GMMA structure. Given the complex fabrication process of metamaterials, some inaccuracies are unavoidable due to the inherent limitations of the fabrication technology used. We have performed the simulation for 5 different test cases and the output graphs are summarized in Figure 3.5

3.5.2 Results

The investigation began with Case-1, featuring four circular rings with 10° split gaps, resulting in dual-band absorption with a bandwidth of 3.5 THz and absorption >90%. In Case-2, the output is almost similar to Case-1 but the absorption peak was higher at 97.3%. In Case-3, thinner resonant structures were used and a fishnet pattern replaced the uniform graphene sheet. The bandwidth remained the same as in Case-1 but the peak absorption increased to 99.1%, the highest observed. Case-4 showed the lowest bandwidth of 1.7 THz and produced a single-band output. Lastly, Case-5 achieved the best performance with a bandwidth twice as wide as the previous cases. It resulted in triple-band absorption, with a bandwidth of 7.69 THz (>90%) ranging from 2.5 THz to 10.19 THz and a peak absorption of 98.9%. These results, all at 0.5 eV are summarized in Table 2.6 and the outputs are shown in Figure 3.5.

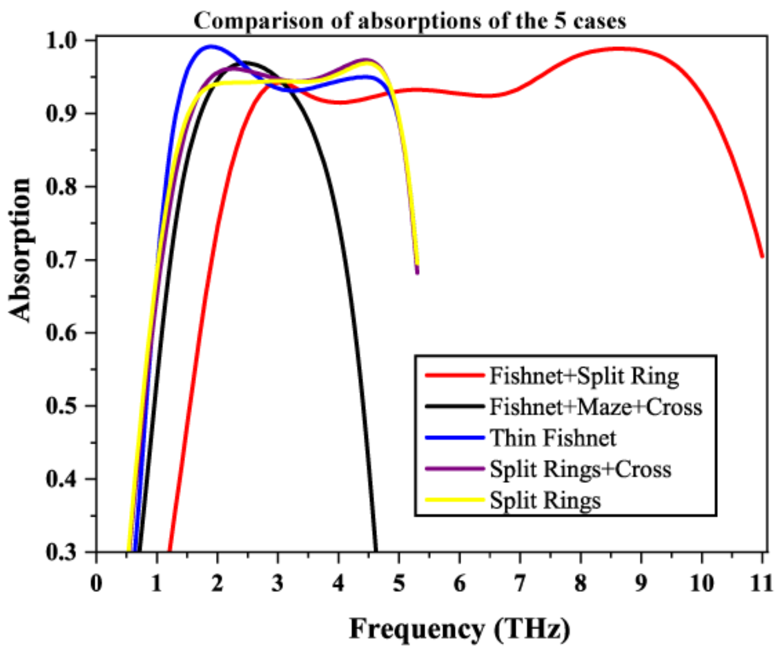

Figure 3.5: Absorption of all 5 cases at 0.5 eV showing different bandwidth for different cases.

The frequency bandwidth in Case-5 is 8 THz (>80%), ranging from 2.1 THz to 10.1 THz, and bandwidth is 9.1 THz (>70%) at 1.9 THz-11 THz shown in Figure 3.5.

Table 3.2: Comparison of different results of absorption achieved and their corresponding bandwidths for 5 different test cases.

Sl	Structure	Bandwidth (THz)	Freq Range (THz)	Absorption	Highest Absorption
1.	Split Rings	3.5	1.5 - 5	>90%	96.9%
2.	Split Rings+Cross	3.6	1.4 - 5	>90%	97.3%
3.	Thin Fishnet+Split Rings+Cross	3.5	1.4 – 4.9	>90%	99.1%
4.	Fishnet+Maze+Cross	1.7	1.8 – 3.5	>90%	96.9%
5.	Fishnet+Split Ring	7.69	2.5 – 10.19	>90%	98.9%

The Table 2.7 presented gives the relationship between the structural parameters and bandwidth and efficiency. This analysis also included an examination of the bandwidth variations across different parameter configurations, as outlined in Table 2.7. To measure these changes, we used the formula

$$B_{deviation} = \left(\frac{B_{variable} - B_{based}}{B_{based}}\right) \times 100\%$$

Here, B_{based} represents the bandwidth associated with the optimized parameters from the simulation, $B_{variable}$ denotes the bandwidth corresponding to various parameter variations from the simulation, and $B_{deviation}$ quantifies the percentage deviation between the optimized and simulated bandwidths.

The simulation results for Case-5, shown in Table 2.7, explore the effects of the varying resonant structures parameters. These parameters include the fishnet structure, that is, the split gaps for the rectangular ring g, the circular ring a, and their thicknesses w and b respectively. The gap g varies between 1μm to 4μm. As g increases, the frequency bandwidth narrows,

Table 3.3: Comprehensive study of bandwidth and efficiency with the changes of structural parameters.

Sl	**Structure Parameter**	**Value**	**BW (THz)**	**BW Deviation (%) (when absorption > 90%)**	**Max Absorbance (%)**
1	g	1 µm	7.69	Optimized structure	98.80%
		2 µm	7.4	3.77	99.94%
		3 µm	7.2	6.37	99.89%
		4 µm	6.5	15.47	98.64%
2	a	10°	7.69	Optimized structure	98.80%
		20°	7.2	6.37	99.52%
		30°	7	8.97	99.61%
		40°	6.3	18.07	99.66%
3	g + a	10µm & 10°	7.69	Optimized structure	98.80%
		20µm & 20°	7.2	6.3	99.99%
		30µm & 30°	7.1	6.3	99.18%
		40µm & 40°	3.3	57	95.92%
4	w + b	0.5 µm	N/A	N/A	75.3%
		1 µm	7.69	-	98.80%
		1.5 µm	7.5	2.47	98.1%
		1.8 µm	7	8.97	98.32%

though the peak absorption experiences minor fluctuations. The circular ring's split gap *a* also plays a significant role in absorption, varying from 10° to 40°. While larger values of a enhance peak absorption, they cause the bandwidth to shrink dramatically with greater deviation from the desired range (shown in Table 2.7). Moreover, when both *g* and *a* increase together, the bandwidth deviation from the optimized structure (BW 7.69) decreases. Finally, increasing the thicknesses *w* and *b* results in a steep decline in the bandwidth.

3.6 Possible Fabrication Realization

Maintaining consisting graphene layers, regulating the thickness of the dielectric layers and removing defects during transfer processes are some of the challenges involved in fabricating a graphene-dielectric based metamaterial absorber. The performance of the graphene may also be affected by its sensitivity to external factors like temperature and humidity. Techniques like atomic layer deposition (ALD) for accurate dielectric stacking, chemical vapour deposition (CVD) for high quality graphene synthesis and clean-room conditions to reduce contamination are needed to overcome these challenges. Furthermore, annealing procedures and the use of a polymer support during graphene transfer can be help remove defects and enhance the material's overall stability and functionality.

One of several transition-metal oxides, including VO_2 experiences semiconductor-to-metal transition (SMT) or an insulator-to-metal transition (IMT) at a distinct phase transition temperature. A great deal of research has been done on the physical characteristics of VO_2 and other vanadium oxides at the phase transition area. The micro/nano fabrication technology can be used to create the intended metasurface. Vanadium oxide thin films have been produced using the direct current magnetron sputtering technique on SiO_2 layer. We use DC magnetron sputtering [69] [70] [71] approach to build the VO_x film . The VO_x will be next converted to VO_2 by annealing at low pressure. Chemical etching and photolithography will next be used to create the VO_2 resonator array. Once more, the VO_2 layer should be spin coated to transfer it to SiO_2. In tests, the VO2 can be heated using a hot plate heater positioned on the rear of the ground plane, and the temperature can be carefully monitored using a laser thermometer. Applying bias voltage to the resistive heaters [72] allows for fine control of the VO_2 temperature. Figure 3.6 shows the layer deposition of VO_2 and SiO_2.

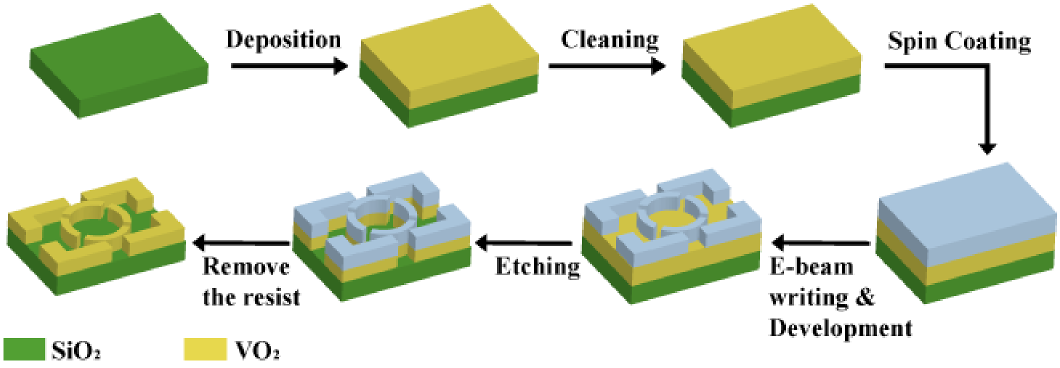

Figure 3.6: Fabrication process of proposed VO_2.

A multi-step procedure used to fabricate graphene, which mostly makes use of the chemical vapour deposition (CVD) techniques, renowned for its dependability and affordability. Because of its remarkable qualities, graphene, a single sheet of carbon atoms organized in a hexagonal lattice structure, is the main material used in this technique. First, the CVD process is used to generate high quality monolayer graphene on a copper or nickel substrate.

The production of a pure graphene sheet, which is necessary for the device's functionality, depends on this phase. A suitable surface for graphene development is provided while preserving cost-effectiveness by using copper or nickel as substrate. Following growth, the graphene layer is placed onto SiO_2, a dielectric medium. The ability to transfer CVD-grown graphene to a variety of additional substrates [41] adds even more versatility to the production process, enabling adjustments according to particular substrate preferences or application needs. After the graphene transfer, a thin dielectric layer is deposited over the structure via spin coating. The dielectric substance, which is then cured in a vacuum oven, is distributed uniformly. The dielectric layer is strengthening throughout the curing process, giving the graphene layer a strong base. For the subsequent graphene layer, the CVD process is repeated, growing a new graphene sheet on a copper substrate before transferring it to pre-existing structure. After that, spin coating is used to apply dielectric layer on the freshly created graphene sheet and it is cured in a vacuum oven. The creation of a robust and effective device structure is ensured by this stacking process, usually tri-layers. The top graphene design is made in the last step of the manufacturing process using traditional lithography and patterned through etching [73]. Finally, this graphene sheet is then transferred to the VO_2 layer. This thorough production method lays the groundwork for the successful fabrication of suggested device by demonstrating the strategic integration of materials and procedures to achieve maximum performance.

Limited pattern design options, design rigidity, material selection concerns, uncontrollability and log-range disorder issues are some of the obstacles that have been faced in the manufacture of metamaterials. Large-scale production of three-dimensional structure is one of the main obstacles to the practical manufactures of metamaterial [42].

3.7 Discussion

This chapter presented a graphene-structured metamaterial absorber, which achieves a broadband spectrum with a bandwidth of approximately 7.69 THz; attaining over 90% efficiency from 2.5 THz to 10.19 THz. Additionally, this structure was fine-tuned to various other geometric configurations to achieve improved bandwidth and absorption. The simulation carried out for 0.2 eV, 0.3 eV, 0.4eV and 0.5 eV. The GMMA displays several remarkable features using VO_2 such as tunability, polarization independence, and robustness against structural changes. Further optimization of the aforementioned structure can lead to even better results. One crucial factor contributing to increased absorption is the addition of circular structures onto the fishnet and vanadium dioxide used as the phase change material.

Additionally, we contrasted our results with existing research, which is compiled in Table 2.8. After choosing the graphene based metamaterial with VO_2 for its phase changing property, we discovered that the bandwidth over 90% ranges from 2.5 THz to 10.19THz. Our results were 1.5 times greater than the highest bandwidth recorded in the literature, outperformed it.

Table 3.4: Comparing bandwidth across different GMMA configurations.

Sl	References	Year	Constituent material	Bandwidth at absorption >90% (THz)	Maximum Absorption
1.	Z. Song et al. [74]	2018	VO_2 and SiO_2	0.33	>95%
2.	H. Lui et al. [75]	2019	Hybrid VO_2	2.0	>80%
3.	M. Wei et al. [76]	2019	VO_2, SiO_2, Au and Si	0.68	98%
4.	J. Zang et al. [77]	2020	VO_2, SiO_2 and Au	0.68	>90%
5.	G. Wu et al. [78]	2021	VO_2, SiO_2 and Au	3.30	>90%
6.	Y. Li et al. [79]	2021	VO2, Quartz and Au	5.10	>90%
7.	R. Zhang et al. [80]	2021	VO_2, SiO_2 and Au	4.10	>90%
8.	H. Feng et al. [81]	2022	VO_2, Topas, SiO_2 and Au	3.4	>90%
9.	J. Wang et al. [82]	2023	VO_2 and graphene	3.37	>90%
10.	This study	2024	Graphene, SiO_2 and VO_2	7.69	98.9%

An ultra-broadband terahertz perfect absorber based on VO_2 consisting of two split rectangles on metallic ground plane that produce an absorption bandwidth of 5.10 THz from 3.03 THz-8.13 THz was recently demonstrated by Yulian Li [79] et al. Furthermore, they observed that the emergence of absorption peaks makes it easy to adjust the thickness of the dielectric layer, hence modifying the THz absorption bandwidth from 3.56 THz-6.46 THz.

Recently, Ruoya Zhang [80] et al. presented a VO_2 based perfect absorber consisting of patterned VO_2 (a combination of cross-shaped and four L-shaped patterns), SiO_2 and Au. According to their simulation results, altering the conductivity of VO_2 can dynamically modify the absorber's peak absorption strength from 3.6% to 100%. A good broadband absorption phenomenon occurs when the conductivity of VO_2 is 2000S/cm. The bandwidth of absorption rate greater than 90% is as wide as 4.10 THz ranging 3.25 THz - 7.35 THz.

Furthermore, an actively adjustable dual-band terahertz perfect absorber was proposed and investigated by Hengli Feng [81] et al. Each cell of the active tunable absorber is made up of metamaterial VO_2 fillet cavities, a TOPAS, SiO_2 and Au film from top to bottom. The absorption bandwidth in our study is insensitive to the polarization angle and can reach 3.4 THz and 3.06 THz with an absorbance more than 90%. By altering the conductivity of the VO_2, the bandwidth can change with TE and TM polarization angles of 70° and 60° respectively.

The aforementioned analysis demonstrates that the proposed graphene-based absorber with phase change material VO_2 and SiO_2 performed better than the published literature, with BW approximately 7.69 THz and maximum absorption approximately 98.9%, across a wide frequency range of 2.5 THz – 10.19 THz, regardless of polarization. Transmission line theory was used to verify the simulation results by examining the link between input impedance and reflection co-efficient, even if the experimental verification is outside the scope of this work.

The innovative aspect of this proposed structure is that GMMA is appropriate for a range of terahertz spectrum applications due to its notable properties, including as tenability, polarization insensitivity and robustness to structural changes. Significant progress in terahertz-frequency-specific GMMA technology has been made with the shown broad bandwidth and tunable capabilities. Additionally, because of its straightforward design, it may be appropriate for electromagnetic interference suppression, antenna design, thermophotovoltaic energy generation system, and solar energy absorption and stealth technology. All things considered, the flexibility and adaptability of GMMA make it a useful tool for meeting demands and obstacles in the development of cutting-edge terahertz technologies. In addition to advancing the technology, this research creates new opportunities for real-world applications.

3.8 Conclusion

In conclusion, we present a terahertz perfect absorber that leverages VO_2 as a phase change material within a traditional dielectric-metal-dielectric tri-layer architecture, specifically incorporating a graphene-VO_2-SiO_2 arrangement. The carefully engineered microstructure of the top layer achieves remarkable absorption efficiency, peaking at 98.9% across 2.5-10.19 THz spectrum centered around 6 THz. Initially, we detailed the underlying mechanisms that drive the high performance characteristics of the structure. Further, we analyze how variations in structural parameters influence absorption efficiency. Thus, our proposed terahertz perfect absorber addresses the non-adjustability limitations of conventional terahertz devices, offering valuable insights for communications, sensing and detection in the terahertz domain, and setting a foundation for future advancements. Despite limitations in bulk fabrication, the structure's clear design and simplicity make it an excellent candidate for various applications including stealth technology, thermophotovoltaic energy system, solar energy capture, terahertz imaging and sensing, and antenna applications.

Chapter 4

Conclusion and Future Prospects

4.1 Conclusion

In this study we developed new terahertz graphene-based tunable broadband absorber of two different structures. An efficient and new method for designing a terahertz absorber is described and examined using graphene layer. In Chapter2, we used materials graphene, SiO_2 and metal, whereas, in Chapter 3, we used VO_2, SiO_2, and graphene. The proposed method is suitable for developing dualband and tripleband absorber in the terahertz range. The optimized structure analyzed in Chapter 2 consists of three circular resonant split-ring of metal index 1.4. In chapter 3, the optimized unit top cell consists of a rectangular split ring and a circular split-ring of VO_2 over graphene sheet. We have achieved 95% absorption with the bandwidth of 3.8THz ranging from 1.1 – 4.9 THz. The other absorber has achieved 98% absorption resulting bandwidth of 7.69 THz ranging from 2.5-10.9 THz. The suggested metamaterial units act as resonant structures gives dualband absorption and with the introduction of phase change material VO_2, results in triple-band absorption with larger bandwidth. This research also shows the variations in frequency bandwidth due to the variations of resonant structures. We have also compares the results and optimized structure with recent related terahertz based works on GMMA with phase change material. Numerical results show that the suggested absorber has adjustable, broadband, polarization-insensitive, and wide-angle features that have successfully achieved higher bandwidth in the range of terahertz.

4.2 Recent advancements and future prospects

Recent advancements in graphene-based metasurfaces have introduced cost-effective solutions for designing antennas, absorbers and sensors operating in the terahertz frequency range. Graphene when integrated with metamaterials and metasurfaces, enables reconfigurability in various aspects, including bandwidth, center frequency, polarization and beam direction. This capability has positioned graphene-based metasurfaces as a transformative technology in photonics, particularly in the THz domain [83]. Graphene-based metamaterial absorbers (GBMA) are an emerging area of research with promising future prospects across various fields. Here are some of their potential applications and future developments:

With the rise of the Internet of things (IoT) [84] and wearable electronics, graphene- based antenna sensors have gained significant interest for applications such as electronic skin devices, implementable medical components, and health monitoring systems. Furthermore, graphene-based metasurfaces have potential applications in designing reflect-array antennas, further broadening their utility in advanced communication systems.

Hybrid materials by combining graphene with 2D materials or plasmonic materials to enhance performance can be another future trend. A water hybrid graphene based metamaterial [85], graphene-Sic hybrid system, use of phase change materials, GST and IST, GST and MXene-based with gold [86] are emerging research trends.

One of the most important properties of graphene is quantum property. The feature is implemented into variety of hybrid materials, including substrates, to allow for specialized tuning of matter to track various quantum signals. Their prospective applications were investigated using nanomaerials and nanotechnology. Graphene, its derivatives and other carbon-based allotropes were chosen because of their unique chemical structure and qualities from the nanoscale to longer lengths, according to specific uses [87].

4.3 Key Challenges and Research Directions

The future development and widespread adoption of graphene-based metamaterial absorber (GBMA) face several key challenges that require attention. These challenges span material fabrication, engineering integration and theoretical advancements. Below is a brief description on these challenges and research directions addressing them:

Traditional manufacturing techniques used to fabricate electromagnetic MMAs include printed circuit board [88], photolithography, magnetron sputtering, chemical vapour deposition(CVD), micro/nano mechanical processing. However, these methods have inherent limitations. The International Committee has identified seven major additive manufacturing techniques [89], three of which have been widely used to manufacture MMAs: material extrusion, vat photopolymerization, and powder bed fusion.

Graphene and its derivatives are prone to environmental degradation when exposed to oxygen, moisture and high temperature, affecting long-term performance. Instability can limit applications in harsh environments such as aerospace or outdoor solar absorbers. Various attempts have been made to prevent inadvertent doping of graphene and limit hysteretic behaviour in graphene-based field effect devices. Thermal annealing, electrical current annealing, plasma cleaning, chloroform treatment and self-assembled monolayers (SAM) are some of the methods used to treat hydrophobic substrate [90]. However, these technologies do not ensure the stability of graphene-based devices in environment conditions. Further caution has to be taken to improve chemical stability without compromising optical properties.

Fabrication process often results in non-uniform graphene layers, defects and grain boundaries that affect optical electronic properties. These imperfections lead to inconsistent performance, especially in applications requiring high precision, such as photodetection.

Finally, despite the challenges, graphene-based possessing intriguing optical characteristics and capabilities, pave an extraordinary avenue for the development of innovative and profound interdisciplinary applications across numerous photonic-related systems. By addressing the above challenges through focused research and innovation, graphene-based metamaterial absorbers have the potential to become a cornerstone technology in photonics, electronics and beyond.

References

[1] R. S. J. I. p. Kshetrimayum, "A brief intro to metamaterials," vol. 23, no. 5, pp. 44-46, 2004.

[2] R. W. Ziolkowski, N. J. I. T. o. A. Engheta, and Propagation, "Metamaterials: two decades past and into their electromagnetics future and beyond," vol. 68, no. 3, pp. 1232-1237, 2019.

[3] A. Ali, A. Mitra, and B. J. N. Aïssa, "Metamaterials and metasurfaces: A review from the perspectives of materials, mechanisms and advanced metadevices," vol. 12, no. 6, p. 1027, 2022.

[4] N. Amiri, K. Forooraghi, Z. J. I. A. Atlasbaf, and W. P. Letters, "A wideband uniplanar polarization independent left-handed metamaterial," vol. 10, pp. 524-527, 2011.

[5] J. W. Park *et al.*, "Multi-band metamaterial absorber based on the arrangement of donut-type resonators," vol. 21, no. 8, pp. 9691-9702, 2013.

[6] N. I. Landy, S. Sajuyigbe, J. J. Mock, D. R. Smith, and W. J. J. P. r. l. Padilla, "Perfect metamaterial absorber," vol. 100, no. 20, p. 207402, 2008.

[7] Z. Shen, S. Li, Y. Xu, W. Yin, L. Zhang, and X. J. P. R. A. Chen, "Three-dimensional printed ultrabroadband terahertz metamaterial absorbers," vol. 16, no. 1, p. 014066, 2021.

[8] S. Banerjee *et al.*, "A new design of a terahertz metamaterial absorber for gas sensing applications," vol. 15, no. 1, p. 24, 2022.

[9] J. Zhu *et al.*, "Ultra-broadband terahertz metamaterial absorber," vol. 105, no. 2, 2014.

[10] P. Yu *et al.*, "Broadband metamaterial absorbers," vol. 7, no. 3, p. 1800995, 2019.

[11] G. P. Kniffin, "Metamaterial Devices for the Terahertz Band," 2009.

[12] Y. Zhang, Y. Shi, and C.-H. J. O. m. e. Liang, "Broadband tunable graphene-based metamaterial absorber," vol. 6, no. 9, pp. 3036-3044, 2016.

[13] J. Rhee, Y. Yoo, K. Kim, Y. Kim, Y. J. J. o. E. W. Lee, and Applications, "Metamaterial-based perfect absorbers," vol. 28, no. 13, pp. 1541-1580, 2014.

[14] H. Ahmadi, S. Vaezi, V. J. Harzand, and R. J. S. s. c. Safian, "Graphene-based terahertz metamaterial absorber for broadband applications," vol. 323, p. 114023, 2021.

[15] Y. Yoo *et al.*, "Flexible and elastic metamaterial absorber for low frequency, based on small-size unit cell," vol. 105, no. 4, 2014.

[16] X. Liu, T. Starr, A. F. Starr, and W. J. J. P. r. l. Padilla, "Infrared spatial and frequency selective metamaterial with near-unity absorbance," vol. 104, no. 20, p. 207403, 2010.

[17] X. Liu, T. Tyler, T. Starr, A. F. Starr, N. M. Jokerst, and W. J. J. P. r. l. Padilla, "Taming the blackbody with infrared metamaterials as selective thermal emitters," vol. 107, no. 4, p. 045901, 2011.

[18] X.-Y. Peng, B. Wang, S. Lai, D. H. Zhang, and J.-H. J. O. e. Teng, "Ultrathin multi-band planar metamaterial absorber based on standing wave resonances," vol. 20, no. 25, pp. 27756-27765, 2012.

[19] Y. Cheng, Y. Nie, R. Gong, and H. J. T. E. P. J.-A. P. Yang, "Multi-band metamaterial absorber using cave-cross resonator," vol. 56, no. 3, p. 31301, 2011.

[20] K. Aydin, V. E. Ferry, R. M. Briggs, and H. A. J. N. c. Atwater, "Broadband polarization-independent resonant light absorption using ultrathin plasmonic super absorbers," vol. 2, no. 1, p. 517, 2011.

[21] M. K. Hedayati, F. Faupel, and M. J. A. P. A. Elbahri, "Tunable broadband plasmonic perfect absorber at visible frequency," vol. 109, pp. 769-773, 2012.

[22] H. Zheng *et al.*, "Tunable dual-band perfect absorbers based on extraordinary optical transmission and Fabry-Perot cavity resonance," vol. 20, no. 21, pp. 24002-24009, 2012.

[23] P. Tuong *et al.*, "Simplified perfect absorber structure," vol. 61, pp. 243-247, 2012.

[24] F. J. I. A. Urbani and W. P. Letters, "Experimental analysis of novel single-sided left-handed metamaterial," vol. 9, pp. 720-723, 2010.

[25] S. Zhang, W. Fan, N. Panoiu, K. Malloy, R. Osgood, and S. J. O. E. Brueck, "Optical negative-index bulk metamaterials consisting of 2D perforated metal-dielectric stacks," vol. 14, no. 15, pp. 6778-6787, 2006.

[26] I. Staude and J. J. N. P. Schilling, "Metamaterial-inspired silicon nanophotonics," vol. 11, no. 5, pp. 274-284, 2017.

[27] Y. Dong and T. J. P. o. t. I. Itoh, "Metamaterial-based antennas," vol. 100, no. 7, pp. 2271-2285, 2012.

[28] L. Mascaretti *et al.*, "Designing Metasurfaces for Efficient Solar Energy Conversion," vol. 10, no. 12, pp. 4079-4103, 2023.

[29] M. A. Jabbar, M. A. Naveed, M. Zubair, M. Q. Mehmood, and Y. J. I. P. J. Massoud, "Wideband polarization insensitive tunable graphene-supported terahertz metamaterial absorber," 2023.

[30] A. Andryieuski and A. V. J. O. e. Lavrinenko, "Graphene metamaterials based tunable terahertz absorber: effective surface conductivity approach," vol. 21, no. 7, pp. 9144-9155, 2013.

[31] L. Ye, F. Zeng, Y. Zhang, and Q. H. J. C. Liu, "Composite graphene-metal microstructures for enhanced multiband absorption covering the entire terahertz range," vol. 148, pp. 317-325, 2019.

[32] R. Kumar, M. Kumar, J. S. Chohan, and S. J. M. T. P. Kumar, "Overview on metamaterial: History, types and applications," vol. 56, pp. 3016-3024, 2022.

[33] M. J. Hossain, M. R. I. Faruque, and M. T. J. P. O. Islam, "Perfect metamaterial absorber with high fractional bandwidth for solar energy harvesting," vol. 13, no. 11, p. e0207314, 2018.

[34] C. S. Kaipa *et al.*, "Enhanced transmission with a graphene-dielectric microstructure at low-terahertz frequencies," vol. 85, no. 24, p. 245407, 2012.

[35] V. Gusynin, S. Sharapov, and J. J. J. o. P. C. M. Carbotte, "Magneto-optical conductivity in graphene," vol. 19, no. 2, p. 026222, 2006.

[36] R. Mishra, R. Panwar, and D. J. I. M. L. Singh, "Equivalent circuit model for the design of frequency-selective, terahertz-band, graphene-based metamaterial absorbers," vol. 9, pp. 1-5, 2018.

[37] L. Sun, J. Sun, B. Yang, X. Gao, H. Long, and Y. J. M. R. E. Shao, "A simplified design of broadband metamaterial absorber covering X-and Ku-band," vol. 6, no. 12, p. 125805, 2020.

[38] D. Smith and D. J. P. r. l. Schurig, "Electromagnetic Wave Propagation in Media with Indefinite Permittivity<? format?> and Permeability Tensors," vol. 90, no. 7, p. 077405, 2003.

[39] I. Chaharmahali, M. Soltani, M. Hoseini, and M. J. O. E. Biabanifard, "Control of terahertz waves for TE and TM modes using graphene-based metamaterials," vol. 59, no. 4, pp. 047101-047101, 2020.

[40] P. Zamzam, P. Rezaei, Y. I. Abdulkarim, O. M. J. O. Daraei, and L. Technology, "Graphene-based polarization-insensitive metamaterials with perfect absorption for terahertz biosensing applications: Analytical approach," vol. 163, p. 109444, 2023.

[41] Y. Hao *et al.*, "The role of surface oxygen in the growth of large single-crystal graphene on copper," vol. 342, no. 6159, pp. 720-723, 2013.

[42] G. Yoon, I. Kim, and J. J. M. E. Rho, "Challenges in fabrication towards realization of practical metamaterials," vol. 163, pp. 7-20, 2016.

[43] L.-Y. Liu, B.-Z. J. I. A. Wang, and W. P. Letters, "A broadband and electrically small planar monopole employing metamaterial transmission line," vol. 14, pp. 1018-1021, 2015.

[44] R. Gao, Z. Xu, C. Ding, L. Wu, and J. J. O. C. Yao, "Graphene metamaterial for multiband and broadband terahertz absorber," vol. 356, pp. 400-404, 2015.

[45] W. Liu, J. Tian, R. Yang, and W. J. C. A. P. Pei, "Design of a type of broadband metamaterial absorber based on metal and graphene," vol. 31, pp. 122-131, 2021.

[46] H. Yu, P. Xiang, Y. Zhu, S. Huang, and X. J. I. P. J. Luo, "Polarization insensitive broadband concentric-annular-strip octagonal terahertz graphene metamaterial absorber," vol. 14, no. 1, pp. 1-6, 2021.

[47] B. Xiao, M. Gu, and S. J. A. o. Xiao, "Broadband, wide-angle and tunable terahertz absorber based on cross-shaped graphene arrays," vol. 56, no. 19, pp. 5458-5462, 2017.

[48] A. Beheshti Asl, D. Pourkhalil, A. Rostami, and H. J. J. o. C. E. Mirtaghioglu, "A perfect electrically tunable graphene-based metamaterial absorber," vol. 20, pp. 864-872, 2021.

[49] S. K. Patel, S. Charola, C. Jani, M. Ladumor, J. Parmar, and T. J. O. M. Guo, "Graphene-based highly efficient and broadband solar absorber," vol. 96, p. 109330, 2019.

[50] B.-X. Wang *et al.*, "Design and experimental realization of triple-band electromagnetically induced transparency terahertz metamaterials employing two big-bright modes for sensing applications," vol. 15, no. 45, pp. 18435-18446, 2023.

[51] J.-H. Deng, H. Xiong, Q. Yang, M. Suo, J.-Y. Xie, and H.-Q. J. I. S. J. Zhang, "Metasurface-based microwave power detector for polarization angle detection," 2023.

[52] B. X. Wang, X. Qin, G. Duan, G. Yang, W. Q. Huang, and Z. J. A. F. M. Huang, "Dielectric-Based Metamaterials for Near-Perfect Light Absorption," p. 2402068, 2024.

[53] W. Lu *et al.*, "Terahertz smart devices based on phase change material VO2 and metamaterial graphene that combine thermally adjustable absorption and selective transmission," vol. 181, p. 111928, 2025.

[54] Z. Fei *et al.*, "Gate-tuning of graphene plasmons revealed by infrared nano-imaging," vol. 487, no. 7405, pp. 82-85, 2012.

[55] P. Tassin, T. Koschny, M. Kafesaki, and C. M. J. N. P. Soukoulis, "A comparison of graphene, superconductors and metals as conductors for metamaterials and plasmonics," vol. 6, no. 4, pp. 259-264, 2012.

[56] M. Liu *et al.*, "A graphene-based broadband optical modulator," vol. 474, no. 7349, pp. 64-67, 2011.

[57] R. Alaee, M. Farhat, C. Rockstuhl, and F. J. O. e. Lederer, "A perfect absorber made of a graphene micro-ribbon metamaterial," vol. 20, no. 27, pp. 28017-28024, 2012.

[58] M. Liu *et al.*, "Terahertz-field-induced insulator-to-metal transition in vanadium dioxide metamaterial," vol. 487, no. 7407, pp. 345-348, 2012.

[59] F. J. P. r. l. Morin, "Oxides which show a metal-to-insulator transition at the Neel temperature," vol. 3, no. 1, p. 34, 1959.

[60] Y. Wu *et al.*, "Review for metamaterials and metasurfaces based on vanadium dioxide phase change materials," vol. 179, p. 111376, 2024.

[61] E. E. J. A. o. Chain, "Optical properties of vanadium dioxide and vanadium pentoxide thin films," vol. 30, no. 19, pp. 2782-2787, 1991.

[62] H. Liu, J. Lu, and X. R. J. N. Wang, "Metamaterials based on the phase transition of VO2," vol. 29, no. 2, p. 024002, 2017.

[63] C. G. J. S. e. m. Granqvist and s. cells, "Transparent conductors as solar energy materials: A panoramic review," vol. 91, no. 17, pp. 1529-1598, 2007.

[64] A. Zylbersztejn and N. F. J. P. R. B. Mott, "Metal-insulator transition in vanadium dioxide," vol. 11, no. 11, p. 4383, 1975.

[65] Q.-Y. Wen *et al.*, "Perfect metamaterial absorbers in microwave and terahertz bands," in *Metamaterial*: Citeseer, 2012.

[66] D. Smith, D. Vier, T. Koschny, C. J. P. R. E. S. Soukoulis, Nonlinear,, and S. M. Physics, "Electromagnetic parameter retrieval from inhomogeneous metamaterials," vol. 71, no. 3, p. 036617, 2005.

[67] T. Badloe, I. Kim, and J. J. S. R. Rho, "Moth-eye shaped on-demand broadband and switchable perfect absorbers based on vanadium dioxide," vol. 10, no. 1, p. 4522, 2020.

[68] K. Shportko, S. Kremers, M. Woda, D. Lencer, J. Robertson, and M. J. N. m. Wuttig, "Resonant bonding in crystalline phase-change materials," vol. 7, no. 8, pp. 653-658, 2008.

[69] S. Chen *et al.*, "Vanadium oxide thin films deposited on silicon dioxide buffer layers by magnetron sputtering," vol. 497, no. 1-2, pp. 267-269, 2006.

[70] S. Barzegar-Parizi, A. Ebrahimi, and K. J. S. R. Ghorbani, "Two bits dual-band switchable terahertz absorber enabled by composite graphene and vanadium dioxide metamaterials," vol. 14, no. 1, p. 5818, 2024.

[71] C. Zhang *et al.*, "Active control of terahertz waves using vanadium-dioxide-embedded metamaterials," vol. 11, no. 5, p. 054016, 2019.

[72] D. E. Anagnostou, D. Torres, T. S. Teeslink, N. J. I. A. Sepulveda, and P. Magazine, "Vanadium dioxide for reconfigurable antennas and microwave devices: Enabling RF reconfigurability through smart materials," vol. 62, no. 3, pp. 58-73, 2020.

[73] T. He, Z. Wang, F. Zhong, H. Fang, P. Wang, and W. J. A. M. T. Hu, "Etching techniques in 2D materials," vol. 4, no. 8, p. 1900064, 2019.

[74] Z. Song, K. Wang, J. Li, and Q. H. J. O. e. Liu, "Broadband tunable terahertz absorber based on vanadium dioxide metamaterials," vol. 26, no. 6, pp. 7148-7154, 2018.

[75] H. Liu, Z.-H. Wang, L. Li, Y.-X. Fan, and Z.-Y. J. S. r. Tao, "Vanadium dioxide-assisted broadband tunable terahertz metamaterial absorber," vol. 9, no. 1, p. 5751, 2019.

[76] Z. Song, M. Wei, Z. Wang, G. Cai, Y. Liu, and Y. J. I. P. J. Zhou, "Terahertz absorber with reconfigurable bandwidth based on isotropic vanadium dioxide metasurfaces," vol. 11, no. 2, pp. 1-7, 2019.

[77] Z. Song and J. J. O. e. Zhang, "Achieving broadband absorption and polarization conversion with a vanadium dioxide metasurface in the same terahertz frequencies," vol. 28, no. 8, pp. 12487-12497, 2020.

[78] G. Wu, X. Jiao, Y. Wang, Z. Zhao, Y. Wang, and J. J. O. E. Liu, "Ultra-wideband tunable metamaterial perfect absorber based on vanadium dioxide," vol. 29, no. 2, pp. 2703-2711, 2021.

[79] Y. Li *et al.*, "Tunable ultra-broadband terahertz perfect absorber based on vanadium oxide metamaterial," vol. 29, no. 25, pp. 41222-41233, 2021.

[80] R. Zhang *et al.*, "Structured vanadium dioxide metamaterial for tunable broadband terahertz absorption," vol. 29, no. 26, pp. 42989-42998, 2021.

[81] H. Feng *et al.*, "Tunable Dual-Broadband Terahertz Absorber with Vanadium Dioxide Metamaterial," vol. 12, no. 10, p. 1731, 2022.

[82] C. Song *et al.*, "Dual-band/ultra-broadband switchable terahertz metamaterial absorber based on vanadium dioxide and graphene," vol. 530, p. 129027, 2023.

[83] M. Esfandiari *et al.*, "Recent and emerging applications of Graphene-based metamaterials in electromagnetics," vol. 221, p. 110920, 2022.

[84] M. Amiri, F. Tofigh, N. Shariati, J. Lipman, and M. J. I. I. o. T. J. Abolhasan, "Review on metamaterial perfect absorbers and their applications to IoT," vol. 8, no. 6, pp. 4105-4131, 2020.

[85] H. Zhang, F. Ling, H. Wang, Y. Zhang, and B. J. O. C. Zhang, "A water hybrid graphene metamaterial absorber with broadband absorption," vol. 463, p. 125394, 2020.

[86] R. Gupta *et al.*, "GST and MXene-Based Highly Sensitive Refractive Index Sensor with Gold Gratings Resonator Operating for Infrared Region," pp. 1-17, 2024.

[87] A. G. Bracamonte, "Advances in Quantum properties of Graphene applied for targeted functional Nanomaterials and Metamaterials," 2023.

[88] D. Shrekenhamer, W. Xu, S. Venkatesh, D. Schurig, S. Sonkusale, and W. J. J. P. r. l. Padilla, "Experimental realization of a metamaterial detector focal plane array," vol. 109, no. 17, p. 177401, 2012.

[89] J.-Y. Lee, J. An, and C. K. J. A. m. t. Chua, "Fundamentals and applications of 3D printing for novel materials," vol. 7, pp. 120-133, 2017.

[90] A. A. Sagade *et al.*, "Highly air stable passivation of graphene based field effect devices," vol. 7, no. 8, pp. 3558-3564, 2015.

Appendix A.

Code used for this project.

```
Ef = [0.2;0.3;0.4;0.5];

A = matrix(length(Ef),100);

for (i = 1:length(Ef)){

switchtolayout;

setmaterial("C (graphene) - broadband","chemical potential (eV)", Ef(i));

run;

A(i,1:100) = 1-transmission('R');

}

f = getdata('R','f');

plot(f/1e12,A(1,1:100),A(2,1:100),A(3,1:100),A(4,1:100),'frequency (THz)', 'Absorbance');

legend('0.2 eV','0.3 eV','0.4 eV','0.5 eV');
```